

## Unveiling Multimessenger Emission from Hidden Cores of Microquasars

YU-JIA WEI (魏煜佳) <sup>1,2</sup> KOHTA MURASE (丸山 浩太) <sup>3,1,2,4</sup> AND B. THEODORE ZHANG (张兵) <sup>5,6</sup>

<sup>1</sup>*Department of Astronomy and Astrophysics, The Pennsylvania State University, 525 Davey Laboratory, University Park, PA 16802, USA*

<sup>2</sup>*Institute for Gravitation and the Cosmos, The Pennsylvania State University, University Park, PA 16802, USA*

<sup>3</sup>*Department of Physics, The Pennsylvania State University, University Park, PA 16802, USA*

<sup>4</sup>*Center for Gravitational Physics and Quantum Information, Yukawa Institute for Theoretical Physics, Kyoto University, Kyoto, Kyoto 606-8502, Japan*

<sup>5</sup>*Key Laboratory of Particle Astrophysics and Experimental Physics Division and Computing Center, Institute of High Energy Physics, Chinese Academy of Sciences, 100049 Beijing, China*

<sup>6</sup>*TIANFU Cosmic Ray Research Center, Chengdu, Sichuan, China*

### ABSTRACT

Microquasars are radio-emitting X-ray binaries accompanied by relativistic jets. They are established sources of 100 TeV gamma rays and are considered promising candidates for cosmic-ray acceleration. Motivated by recent detections of  $\sim 100$  TeV photons from Cygnus X-1 and  $\sim$  PeV photons from Cygnus X-3 by the Large High Altitude Air Shower Observatory (LHAASO), we employ the Astrophysical Multimessenger Emission Simulator (AMES) to model their multimessenger emission considering compact outflow regions as cosmic-ray accelerators, spanning from radio to ultra-high-energy gamma rays. Our results show that the observed  $>$ TeV gamma rays can originate from either  $p\gamma$  or  $pp$  interactions, depending on the location and physical conditions of the emission region, while also reproducing the lower-energy spectra. The different configurations yield unique, observationally testable predictions. In the 0.1 – 10 TeV energy range, where current observations provide only upper limits, they predict either a deep dip, a mild suppression, or a power-law spectrum. Additionally, models involving AU-scale blob regions predict strong variability, while those invoking more extended and static external zones show more stable behavior. We also provide a possible qualitative explanation for the distinct modulation patterns across different energy bands, which relies primarily on changes in the Doppler factor and external  $\gamma\gamma$  absorption. Finally, our neutrino predictions, which properly account for muon and pion cooling effects, reveal a significantly suppressed flux, indicating that detecting these sources may be more challenging than previously anticipated.

*Keywords:* X-ray binary stars (1811) — Jets (870) — Non-thermal radiation sources (1119) — Cosmic rays (329) — Neutrino astronomy (1100)

### 1. INTRODUCTION

Microquasars are radio-emitting X-ray binaries (XRBs) characterized by the presence of relativistic jets, typically observed within the Milky Way or in nearby galaxies (e.g., I. F. Mirabel & L. F. Rodríguez 1999; R. Fender 2001; C. Done et al. 2007; S.-N. Zhang 2013; F. Yuan & R. Narayan 2014, for a review). These systems consist of a compact object, such as a neutron star (NS) or a stellar-mass black hole (BH), accreting material from a companion star. As the accreted matter carries angular momentum, it forms an accretion disk around

the compact object. The disk is the primary source of X-ray emission and drives the formation and collimation of relativistic jets. The jets, in turn, produce non-thermal radiation across a broad range of wavelengths, from radio to gamma-rays.

Previous studies have shown that microquasars exhibit two classical accretion states: the high/soft state and the low/hard state, in order of decreasing luminosity, originally identified in Cygnus X-1 (H. Tananbaum et al. 1972). Persistent jets are generally expected during the low/hard state, while transient ejections occur when the source transitions from the low/hard to the high/soft state (e.g., R. P. Fender et al. 2003). In addition to these compact (AU-scale) jets, extended large-

scale jets are thought to arise from the long-term interaction of steady jets with the interstellar medium (ISM) (e.g., M. Ribó 2005; R. Fender 2006, for a review). Also, it is noted that weak jet activity in the soft state cannot be entirely ruled out (A. Rushton et al. 2012).

XRBS have long been proposed as potential sources of high-energy neutrinos and gamma rays (e.g., F. W. Stecker et al. 1985; T. K. Gaisser & T. Stanev 1985; A. Levinson & E. Waxman 2001; C. Distefano et al. 2002; M. M. Reynoso & G. E. Romero 2009). Recently, microquasars have been established as 100 TeV photon emitters. Gamma-ray emission above 100 TeV from the extended jet of V4641 Sgr has been detected by the High Altitude Water Cherenkov (HAWC) Observatory (R. Alfaro et al. 2024) and H.E.S.S. (A. Acharyya et al. 2025). Furthermore, the Large High Altitude Air Shower Observatory (LHAASO) has reported gamma-ray emission up to  $\sim 100$  TeV from the microquasars SS 433, V4641 Sgr, GRS 1915+105, MAXI J1820+070, and Cygnus X-1 (LHAASO Collaboration 2025a). These observations indicate that microquasars are highly efficient particle accelerators capable of energizing particles beyond one PeV ( $> 10^{15}$  eV). Theoretical studies further suggest that microquasars may contribute to cosmic-ray spectra near the knee ( $\sim 3$  PeV) (e.g., A. J. Cooper et al. 2020; B. T. Zhang et al. 2025; M. Kachelrieß & E. Lammert 2025).

However, the origin of the non-thermal gamma rays in microquasars remains uncertain. Two primary mechanisms have been proposed: leptonic processes (e.g., G. Dubus et al. 2010a; A. A. Zdziarski et al. 2012, 2018), including synchrotron radiation and inverse Compton (IC) scattering from relativistic electrons, and hadronic processes (e.g., W. Bednarek 2005; M. M. Reynoso et al. 2008; P. Baerwald & D. Guetta 2013), involving proton synchrotron radiation, inelastic hadronuclear ( $pp$ ) collisions, Bethe-Heitler (BH) pair production, and photomeson ( $p\gamma$ ) interactions. Hadronic emission is of particular interest because photons above 0.1 PeV, which are linked to cosmic rays (CRs) and neutrinos, are not easily explained by purely leptonic processes. While some lepto-hadronic models (e.g., C. Pepe et al. 2015; S. S. Kimura et al. 2020; D. Kantzas et al. 2021; R. Kuze et al. 2025; J. Carpio et al. 2025) have been developed to identify the dominant mechanism, most neglect crucial cooling processes such as muon and pion cooling, which can substantially affect the production of high-energy photons and neutrinos.

To address these limitations, we extend the Astrophysical Multimessenger Emission Simulator (AMES), which has been developed in a sequence of papers by a

part of the authors (e.g., K. Murase 2012; K. Murase et al. 2015; K. Murase 2018, 2022; B. T. Zhang & K. Murase 2023; K. Murase 2024), to self-consistently model both leptonic and hadronic processes responsible for multimessenger emission from microquasars. Motivated by recent detections of  $\sim 100$  TeV photons from Cygnus X-1 (LHAASO Collaboration 2025a) and  $\sim$  PeV photons from Cygnus X-3 (LHAASO Collaboration 2025b), we investigate their potential multimessenger emission in this work using AMES. To comprehensively model both the 0.1-1 PeV and lower-energy band photons, we develop three distinct scenarios, each representing different physical conditions of the emission region: the jet-core model (Scenario A), the stellar-wind interaction model (Scenario B), and the extended-jet model (Scenario C). In each scenario, we assume two uniform emission zones, providing a framework for predicting the broadband photon and neutrino spectra from microquasars.

In Sect. 2, we present the theoretical framework, including the binary geometry, three physical scenarios, the numerical methods implemented in AMES, the origins of external seed photons, external absorption processes, and particle escape timescales. In Sect. 3, we model the multimessenger emission from the microquasars Cygnus X-1 and Cygnus X-3 to investigate the production of high-energy photons and neutrinos, assessing their potential for accelerating CRs. In Sect. 4, we investigate the energy-dependent orbital modulation arising from variations in the Doppler factor and external  $\gamma\gamma$  annihilation. In Sect. 5, we further examine the influence of muon and pion cooling in each scenario and predict the expected number of neutrino events for current and next-generation neutrino detectors. Finally, we summarize our works in Sect. 6.

We use notations as  $Q_x = Q/10^x$  in the CGS unit. Quantities in the laboratory (lab) frame are unprimed, while those in the co-moving frame are primed. Especially, we adopt the notation  $E = \delta\varepsilon'$ , where  $E$  is the lab frame energy,  $\varepsilon'$  is the co-moving frame energy, and  $\delta$  is the Doppler factor. In this work, we do not distinguish between the lab and observer frames since microquasars reside in the Milky Way or nearby galaxies.

## 2. MODEL

The binary system related to the microquasar consists of a donor star (e.g., a massive O-type star or Wolf-Rayet star) and a compact object (e.g., a black hole or neutron star). Fig. 1 illustrates this system's geometry. For clarity, the schematic picture depicts radiation produced via leptonic and hadronic processes within a single spherical relativistic blob (a jet blob) moving with



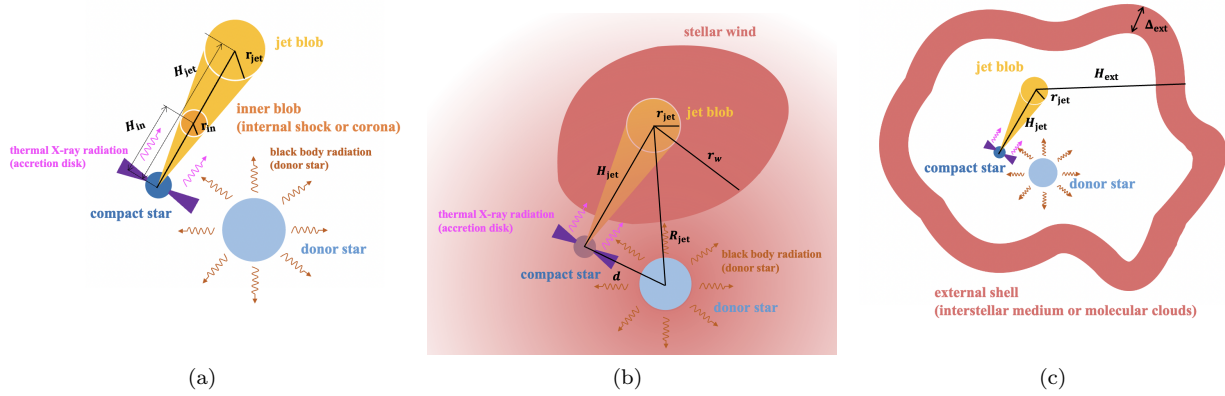


**Figure 2.** Schematic pictures of the three physical configurations modeled in this work. **Panel (a):** Scenario A consists of an inner blob, originating from either the corona or an internal shock, and a jet blob, produced by either an internal or termination shock. Both blobs lie along the same direction but are located at different heights and move with distinct velocities. **Panel (b):** Scenario B features a primary jet emission region surrounded by the dense stellar wind environment of the companion star. In the static external emission zone, charged particles escaping from the jet interact with the stellar wind. **Panel (c):** Scenario C considers the contribution from the extended jet. Within the large-scale, static external shell, particles that have escaped from the jet blob interact with the surrounding parsec-scale environment.

in Fig. 2(b), we assume that this external region is co-located with the jet blob and has a radius  $r_w$ . We further assume  $r_w = R_{jet}$ , where  $R_{jet}$  denotes the distance between the jet blob center and the donor star. The number density of the external region,  $n_{p,ext}$ , is assumed to be constant and is related to the stellar wind density at  $R_{jet}$ .

- **Extended-Jet Model (Scenario C):** Extended parsec-scale jets producing TeV gamma rays have been observed in microquasar systems such as SS 433 and V4641 Sgr (A. U. Abeysekara et al. 2018; R. Alfaro et al. 2024; LHAASO Collaboration 2025a). Motivated by these observations and the theoretical studies investigating their origin (e.g., S. S. Kimura et al. 2020; J. Carpio et al. 2025; Y. Ohira 2025), we propose Scenario C, which considers contributions from large-scale jet structures. In addition to the jet blob, we introduce a static external region with total mass  $M_{p,ext}$  and number density  $n_{p,ext}$ . Within this region, charged particles escaping from the jet blob interact with the surrounding parsec-scale environment (e.g., molecular clouds or the interstellar medium), as illustrated in Fig. 2(c). The external region is modeled as a spherical shell with radius  $H_{ext}$  and width  $\Delta_{ext}$ . This scenario also favors  $pp$  interactions; however, due to its much larger spatial scale compared to Scenario B, it is expected to produce more persistent, non-modulated radiation with reduced variability.

Given the compact size of the radiative region, Scenario A naturally predicts strong variability. In contrast, Scenarios B and C involve more extended and static external zones and thus exhibit more stable behavior.

### 2.1. Numerical Methods

We further develop AMES to numerically calculate the multimessenger emission (including photons and neutrinos) from microquasars. In this framework, the inner blob (which could be a moving corona) is treated identically to the jet blob, differing only in its parameter values. The external region is treated similarly, with the key distinctions being that it is static and its injected particles originate from those escaped the jet blob.

We assume that the injected particle distribution for species  $a$  (e.g., electrons or protons) in the blob follows a power law with a minimum Lorentz factor  $\gamma'_{a,min}$  and an exponential cutoff at  $\gamma'_{a,max}$ :

$$\dot{N}'_{a,inj}(\gamma'_a) = \begin{cases} K'_a \gamma'^{-s_a} \exp\left(-\frac{\gamma'}{\gamma'_{a,max}}\right), & \gamma' \geq \gamma'_{a,min} \\ 0, & \text{otherwise} \end{cases} \quad (3)$$

where  $\dot{N}'_{a,inj}$  denotes the number of particles  $a$  injected per second in the blob co-moving frame,  $K'_a$  is the normalization constant, and  $s_a$  is the spectral index.

The values of  $\gamma'_{min}$  and  $\gamma'_{max}$  vary for different particle species depending on the specific physical conditions. Considering the acceleration process, the maximum Lorentz factor can be estimated by balancing the acceleration timescale  $t'_{acc}$  and the cooling timescale  $t'_c$  within the dynamical timescale  $t'_{dyn} = r'/v_j$  in the blob

co-moving frame; that is,

$$t'_{\text{acc}} = \min(t'_{\text{dyn}}, t'_c). \quad (4)$$

The acceleration timescale at the blob co-moving frame can be written as

$$t'_{\text{acc}} = \eta_{\text{acc}} \frac{r'_L}{c}, \quad (5)$$

where  $r'_L = \gamma'_a m_a c^2 / (eB')$  is the gyration radius,  $B'$  is the magnetic field in the blob co-moving frame,  $m_a$  is the mass of a single particle  $a$ , and  $\eta_{\text{acc}} \simeq \xi_B \beta_j^{-2}$  with  $\xi_B \gtrsim 1$ , hereafter referred to as the acceleration parameter, is a dimensionless parameter characterizing the specifics of the particle acceleration mechanism (J. P. Rachen & P. Mészáros 1998). Specifically, for electrons, both synchrotron and IC cooling can be important. As an example, the synchrotron cooling timescale is given by

$$t'_{\text{syn}} = \frac{6\pi m_e c}{\sigma_T B'^2 \gamma'_e} \simeq 7.7 \times 10^4 \text{ s } B_1^{-2} \gamma'_{e,2}^{-1}. \quad (6)$$

The maximum electron energy,  $\varepsilon'_{e,\text{max}} = \gamma'_{e,\text{max}} m_e c^2$ , can be determined by equating the acceleration timescale  $t'_{\text{acc}}$  to the synchrotron cooling timescale  $t'_{\text{syn}}$ , yielding

$$\varepsilon'_{e,\text{max}} = \sqrt{\frac{6\pi m_e^2 c^4}{\eta_{\text{acc}} \sigma_T B'}} \simeq 20 \text{ TeV } \eta_{\text{acc}}^{-1/2} B_1^{-1/2}. \quad (7)$$

For protons, radiative cooling is generally less significant. Their maximum energy can be estimated by equating the acceleration timescale to the dynamical timescale  $t'_{\text{dyn}}$ , giving

$$\varepsilon'_{p,\text{max}} = \frac{eB'r'}{\eta_{\text{acc}} \beta_j} \simeq 300 \text{ TeV } \eta_{\text{acc}}^{-1} B_1^{-1} r'_{11} \beta_j^{-1}. \quad (8)$$

The magnetic field  $B'$  in the blob co-moving frame is given by

$$\frac{B'^2}{8\pi} = \frac{\epsilon_B L'_{a,\text{inj}}}{\epsilon_a 4\pi r'^2 \beta_j c}, \quad (9)$$

where  $\epsilon_B$  is the fraction of blob energy transferred into magnetic energy, and  $\epsilon_a$  is the fraction of blob energy transferred to particles  $a$ . The injected isotropic-equivalent kinetic luminosities of particle species  $a$  in the co-moving frame  $L'_{a,\text{inj}}$  are given by:

$$L'_{a,\text{inj}} = \int_{\gamma'_{a,\text{min}}}^{\gamma'_{a,\text{max}}} \dot{N}'_a(\gamma'_a) (\gamma'_a - 1) m_a c^2 d\gamma'_a. \quad (10)$$

The injection luminosity can also be expressed as

$$L'_{a,\text{inj}} = \frac{2\epsilon_a P_j}{\Gamma_j^2 \delta_j^4}, \quad (11)$$

where  $P_j$  is the blob power in the lab frame. Note that the sum of the energy fractions satisfies  $\epsilon_B + \sum \epsilon_a \lesssim 1$ , which ensures energy conservation within the system. Here, we consider two fractions of the particle energy partition,  $\epsilon_e$  and  $\epsilon_p$ , which represent the fractions of total energy transferred to electrons and protons, respectively. Also, all microphysical efficiency parameters ( $\epsilon_p$ ,  $\epsilon_e$ , and  $\epsilon_B$ ) used in our models are less than 0.1.

It is noted that the proton number density in the blob is constrained by the total injected proton luminosity. The upper limit on the proton number density,  $n'_{p,\text{ul}}$ , in the blob co-moving frame is given by:

$$n'_{p,\text{ul}} = \frac{3L'_{p,\text{inj}}}{4\pi r'^2 m_p c^3} \simeq 5.3 \times 10^6 \text{ cm}^{-3} L'_{p,\text{inj},37} r'_{11}{}^{-2}. \quad (12)$$

In this work, we set the proton number density entrained in the blob to be 10% of this upper limit, i.e.,  $n'_{p,\text{jet}} = 0.1 n'_{p,\text{ul}}$ .

In our calculations, we consider both leptonic and hadronic processes. Leptonic processes mainly include synchrotron radiation, IC scattering, involving both synchrotron self-Compton (SSC) and external inverse Compton (EIC) processes, and  $\gamma\gamma$  annihilation. Hadronic processes mainly include proton synchrotron radiation, decay processes,  $pp$  interactions,  $p\gamma$  processes, and BH processes. These lepto-hadronic processes can be modeled by solving a series of coupled transport equations for photons, electrons, neutrinos, neutrons, protons, muons, and pions in the blob co-moving frame. The transport equation for particle species  $a$  in the co-moving frame is given by

$$\begin{aligned} \frac{\partial n'_{\varepsilon'_a}}{\partial t'} &= -n'_{\varepsilon'_a} \mathcal{A}'_a(\varepsilon'_a) \\ &+ \int d\varepsilon'^* n'_{\varepsilon'^*} \mathcal{B}'_{a \rightarrow a}(\varepsilon'_a, \varepsilon'^*) \\ &+ \sum_b \int d\varepsilon'_b n'_{\varepsilon'_b} \mathcal{C}'_{b \rightarrow a}(\varepsilon'_a, \varepsilon'_b) \\ &+ \dot{n}'_{a,\text{inj}}(\varepsilon'_a), \end{aligned} \quad (13)$$

where  $n'_{\varepsilon'_a}$  is the differential number density at energy  $\varepsilon'_a$ ,  $\mathcal{A}'_a(\varepsilon'_a)$  is the total interaction rate at energy  $\varepsilon'_a$  including the escaping of particles  $a$ ,  $\mathcal{B}'_{a \rightarrow a}(\varepsilon'_a, \varepsilon'^*)$  denotes the self-production rate of particles  $a$  with energy  $\varepsilon'_a$  generated from the same type of particles with energy  $\varepsilon'^*$ ,  $\mathcal{C}'_{b \rightarrow a}(\varepsilon'_a, \varepsilon'_b)$  represents the production rate of particles  $a$  with energy  $\varepsilon'_a$  originating from particles  $b$  with energy  $\varepsilon'_b$ ,  $\dot{n}'_{a,\text{inj}}(\varepsilon'_a) = \dot{N}'_{a,\text{inj}}(\varepsilon'_a) / V'$  is the source injection rate at energy  $\varepsilon'_a$ , and  $V'$  is the volume of the system in the co-moving frame.

### 2.1.1. Muon/Pion Cooling

Pions, which subsequently decay into muons, are generated through either  $pp$  or  $p\gamma$  interactions. The production of neutrinos and photons from the decay of secondary particles (muons and pions) can be suppressed if the system's dynamical time is shorter than the particle's lifetime. This effect is particularly significant for high-energy particles due to relativistic time dilation. Besides, compared to [B. T. Zhang & K. Murase \(2023\)](#), we additionally include synchrotron processes of muons and pions, and IC processes of muons, which could affect both photons and neutrinos.

We adopt a classical treatment for synchrotron radiation, where the equations governing muons and pions are similar to those for electrons. The energy losses of the particle species  $a$  due to synchrotron radiation are

$$\frac{d\varepsilon'_{a,\text{syn}}}{dt'} = -\frac{4\sigma_T Z^4 U'_B}{3m_e^2 c^3} \varepsilon_a'^2 \left(\frac{m_e}{m_a}\right)^4, \quad (14)$$

where  $U'_B = B'^2/8\pi$  is the magnetic energy density,  $Z$  is the charge number of the particle  $a$ , and  $m_a$  is the mass of the particle  $a$ . The corresponding synchrotron emissivity for the particle species  $a$  is ([B. T. Zhang et al. 2021](#))

$$\frac{dn'_{a,\text{syn}}}{dt' d\varepsilon'_{\text{ph}}} = \frac{1.81\sqrt{3}Z^3 e^3 B'}{hm_a c^2 \varepsilon'_{\text{ph}}} \int d\gamma'_a n'_a(\gamma'_a) G\left(\frac{\varepsilon'_{\text{ph}}}{\varepsilon'_c}\right), \quad (15)$$

where

$$G(x) = \frac{e^{-x}}{\sqrt{x^{-2/3} + (3.62/\pi)^2}}, \quad \text{and } \varepsilon'_c = \frac{3ZehB'\gamma_a'^2}{8\pi m_a c}. \quad (16)$$

Here,  $\varepsilon'_{\text{ph}}$  is the photon energy in the co-moving frame, and  $n'_a(\gamma'_a) = dn'_a/d\gamma'_a$  is the differential number density of the particle  $a$  in the co-moving frame.

For IC scattering of muons, we employ a cross section analogous to that of electrons since both of them are fermions. The emissivity of IC scattering assumed the isotropic particles  $a$  and isotropic target photons is ([G. R. Blumenthal & R. J. Gould 1970](#); [B. T. Zhang et al. 2021](#))

$$\begin{aligned} \frac{dn'_{a,\text{IC}}}{dt' d\varepsilon'_{\text{ph}}} &= \frac{3\sigma_T c}{16\pi} \left(\frac{m_e}{m_a}\right)^2 \\ &\times \int d\gamma'_a n'_a(\gamma'_a) \frac{1}{\gamma_a'^2} \int d\varepsilon' \frac{1}{\varepsilon'} \frac{dn'_{\text{ph}}}{d\varepsilon'} f(q, w), \end{aligned} \quad (17)$$

where

$$\begin{aligned} f(q, w) &= 2q \ln q + (1+2q)(1-q) + \frac{1}{2} \frac{(wq)^2}{1+wq} (1-q), \\ w &= \frac{4\varepsilon'_a \gamma'_a}{m_a c^2}, \quad \text{and } q = \frac{\varepsilon'_{\text{ph}}}{w(\varepsilon'_a - \varepsilon'_{\text{ph}})}. \end{aligned} \quad (18)$$

Here,  $dn'_{\text{ph}}/d\varepsilon'$  represents the differential number density of target photons. This includes external photon fields and internally accumulated photons from prior processes such as synchrotron emission. The energy losses of the particle  $a$  due to IC scattering are

$$\frac{d\varepsilon'_{a,\text{IC}}}{dt'} = -V' \int d\varepsilon'_{\text{ph}} (\varepsilon'_{\text{ph}} - \varepsilon') \frac{dn'_{a,\text{IC}}}{dt' d\varepsilon'_{\text{ph}}}, \quad (19)$$

where  $V'$  is the volume of the system in the co-moving frame, and  $dn'_{a,\text{IC}}/(dt' d\varepsilon'_{\text{ph}})$  represents the differential number density of IC scattered photons generated by a single particle  $a$  with  $\gamma'_a$ , which could be taken from Eq. 17 considering  $n'_a(\gamma'_a)$  is a delta function.

Although these processes (i.e., synchrotron processes of muons and pions, and IC processes of muons) can contribute to photon production, their contributions are minor compared to other mechanisms. More importantly, these processes cool muons and pions, which in turn suppress the neutrino generated by  $p\gamma$  processes. This cooling effect is particularly significant for neutrinos above TeV, as shown in Fig. 8.

### 2.2. Origin of External Seed Photons

In this work, we mainly consider two kinds of external photon fields. The first is the thermal emission from the donor star, which we model as a blackbody with radius  $R_*$ , temperature  $T_*$ , and luminosity  $L_*$ . We treat the stellar frame as the lab frame since the orbital velocity of the donor star is negligible compared to the blob's velocity. As the blob moves with velocity  $\beta_j$ , the stellar radiation field is boosted in the blob co-moving frame. This boost is described by the Doppler factor  $\delta_*$ , which is

$$\delta_* = \frac{1}{\Gamma_j (1 - \beta_j \vec{e}_* \cdot \vec{e}_{\text{jet}})}. \quad (20)$$

The differential number density of the blackbody photons from the donor star, as measured at the location of the blob in the stellar (lab) frame, is given by ([A. A. Zdziarski et al. 2012](#))

$$\frac{dn_{\text{ph},*}}{dE_{\text{ph},*}} = \frac{2\pi}{c^3 h^3} \left(\frac{R_*}{R}\right)^2 \frac{E_{\text{ph},*}^2}{\exp(E_{\text{ph},*}/kT_*) - 1}, \quad (21)$$

where  $E_{\text{ph},*} = \delta_* \varepsilon'_{\text{ph},*}$  is the photon energy in the lab frame,  $k$  is the Boltzmann constant, and  $h$  is the Planck constant.

Photons from the accretion disk provide another potential source of external seed photons. The differential number density of the disk's photon field, evaluated at the blob's position in the lab frame, is

$$\frac{dn_{\text{ph,disk}}}{dE_{\text{ph,disk}}} = \frac{L_{E_{\text{ph,disk}}}}{4\pi H^2 c E_{\text{ph,disk}}}, \quad (22)$$

where  $E_{\text{ph,disk}} = \delta_{\text{disk}} \epsilon'_{\text{ph,disk}}$  is the energy of disk photons in the lab frame,  $\delta_{\text{disk}} = [\Gamma_j(1 - \beta_j)]^{-1}$  is the related Doppler factor,  $L_{E_{\text{ph}}}$  is the differential isotropic-equivalent luminosity of disk photons in the lab frame, and  $H = H'/\Gamma_j$  is the location of the blob in the lab frame. The photons emitted from the accretion disk are predominantly observed in the X-ray band. Therefore, the number density of these target photons can be estimated based on the observed X-ray spectrum. This is expressed by  $E_{\text{ph}} L_{E_{\text{ph}}} = 4\pi d_L^2 E_{\text{ph}} F_{E_{\text{ph}}}$ , where  $E_{\text{ph}} F_{E_{\text{ph}}}$  is the observed flux at energy  $E_{\text{ph}}$ , and  $d_L$  is the distance from the source to the observer.

Note that in Scenario A, the jet blob additionally interacts with photons from the inner blob, while in Scenarios B and C, the external region also includes target photons from the jet blob. Since  $dn_{\text{ph}}/dE_{\text{ph}}$  is a relativistic invariant (G. R. Blumenthal & R. J. Gould 1970), we can easily rewrite Eqs. 21 and 22 to be in the co-moving frame.

### 2.3. External Absorption

Here, we consider two types of external absorption (EB) mechanisms: (i) free-free absorption, which occurs when radio photons emitted from the radiation region interact with particles in the stellar wind while propagating toward the observer, and (ii) external  $\gamma\gamma$  annihilation, which takes place when high-energy photons interact with target photons along the line-of-sight.

#### 2.3.1. Free-Free Absorption from Winds

We assume that the stellar wind from the donor star is smooth and spherically symmetric, following a standard velocity profile in the lab frame (e.g., D. Schaerer 1996),

$$v_w(r) = v_{w,\infty} \left(1 - \frac{r_0}{r}\right)^\beta, \quad r > R_\star, \quad (23)$$

where  $r$  is the distance from the center of the donor star,  $v_{w,\infty} = \sqrt{2GM_\star/R_\star}$  is the terminal wind velocity,  $R_\star$  is the radius of the donor star,  $M_\star$  is the mass of the donor star, and  $\beta$  parametrizes the wind acceleration. The constant  $r_0$  is defined as

$$r_0 = R_\star \left[1 - \left(\frac{v_{w,\star}}{v_{w,\infty}}\right)^{1/\beta}\right], \quad (24)$$

where  $v_{w,\star} = \sqrt{\frac{kT_\star}{\mu m_H}}$  is the initial wind velocity at the stellar surface,  $T_\star$  is the temperature of the donor star,

$\mu \simeq 1$  is the mean molecular weight, and  $m_H$  is the hydrogen mass. Given that the blob velocity  $\beta_j$  greatly exceeds the stellar wind velocity, the stellar wind frame is taken as the lab frame. The particle number density at a distance  $r$  is determined by the continuity equation,

$$n_w(r) = \frac{\dot{M}_w}{4\pi r^2 \mu m_H v_w(r)}, \quad (25)$$

where  $\dot{M}_w$  is the stellar mass-loss rate. The local wind temperature is determined by the balance among radiative heating, cooling, and advection processes. Considering the irradiation of X-rays from the accretion disk, we adopt a characteristic wind temperature of  $T_w = 10^6$  K (e.g., A. Szostek & A. A. Zdziarski 2007).

Then, for simplicity and by neglecting the detailed dependence on metallicity, the characteristic optical depth for free-free absorption in the stellar wind can be approximated as (e.g., K. Murase 2024)

$$\tau_{\text{ff}} \simeq 8.5 \times 10^{-28} \nu_{\text{ph},10}^{-2.1} T_{w,4}^{-1.35} R [n_w(R)]^2, \quad (26)$$

where  $\nu_{\text{ph}} = E_{\text{ph}}/h$  is the photon frequency in the lab frame, and  $R$  is the distance between the donor star and the emission region. The suppression factor due to free-free absorption is given by

$$f_{\text{sup,ff}} = \exp(-\tau_{\text{ff}}). \quad (27)$$

#### 2.3.2. External $\gamma\gamma$ annihilation

We consider external  $\gamma\gamma$  annihilation for the blob, with target photons originating from both the donor star and the accretion disk. In Scenario A, for the jet blob, we additionally include contributions from the inner blob, while for the inner blob, we account for interactions with photons from the jet blob.

The differential absorption opacity for a gamma-ray photon of energy  $E_{\text{ph}}$  propagating along the direction  $\vec{e}_{\text{obs}}$  is estimated as

$$\tau_{\gamma\gamma} = R \int dE_{\text{ph,t}} \sigma_{\gamma\gamma} [1 + \cos\psi] \frac{dn_{\text{ph,t}}}{dE_{\text{ph,t}}}(R_{\gamma\gamma}), \quad (28)$$

where  $\sigma_{\gamma\gamma}$  is the pair-production cross section (R. J. Gould & G. P. Schröder 1967),  $R$  is the distance between the radiation region and the donor star (representing the path length over which external  $\gamma\gamma$  annihilation is evaluated along the line-of-sight),  $R_{\gamma\gamma}$  is the distance between the midpoint of the annihilation region and the source of target photons,  $\frac{dn_{\text{ph,t}}}{dE_{\text{ph,t}}}(R_{\gamma\gamma})$  is the differential target photon number density at that location, and  $\psi$  is the angle between the line-of-sight and the direction of the target photons. The suppression factor due to the external  $\gamma\gamma$  annihilation is given by

$$f_{\text{sup},\gamma\gamma} = \exp(-\tau_{\gamma\gamma}). \quad (29)$$

#### 2.4. Escape Timescales of Charged Particles

In all scenarios, we consider the escape of charged particles, characterized by distinct escape timescales. Two separate regions are defined: the accelerator (i.e., the jet blob and/or inner blob) and the reservoir (i.e., the external region), each with different escape timescales.

In the accelerator, the escape timescale for charged particles in the lab frame is

$$t_{\text{esc}} = r/v_j, \quad (30)$$

where  $r$  is the radius of the blob in the lab frame.

In the external regions of Scenarios B and C, the injected charged particles originate from those escaping the jet blob. The escaping efficiency of the charged particles in the jet blob can be estimated as

$$f_{\text{esc}} = \min\left(1, \frac{t_c}{t_{\text{dyn}}}\right), \quad (31)$$

where  $t_c$  is the cooling timescale. Therefore, the luminosity of charged particles  $a$  (e.g., electrons and/or protons) at the external region in the lab frame can be written as

$$L_{a,\text{ext}} = \frac{\delta_j^4}{2\Gamma_j^2} f_{\text{cov}} f_{\text{esc}} L'_{a,\text{inj}}, \quad (32)$$

where  $f_{\text{cov}} = \Delta\Omega_{\text{ext}}/(4\pi)$  is the covering factor,  $\Delta\Omega_{\text{ext}}$  denotes the solid angle subtended by the external blob as seen from the jet blob, and  $L'_{a,\text{inj}}$  is the injected luminosity for particle species  $a$  in the blob co-moving frame.

In the reservoir, considering diffusion escape, the escape timescale for charged particles  $a$  in the lab frame is

$$t_{a,\text{esc}} = \max\left(t_{a,\text{diff}}, \frac{r_{\text{ext}}}{c}\right), \quad (33)$$

where  $t_{a,\text{diff}} = r_{\text{ext}}^2/(6D)$  is the diffusion timescale,

$$D = \frac{cr_{\text{ext}}}{3} \times \left[ 4 \left( \frac{E_a}{E_{c,\text{diff}}} \right)^2 + 0.9 \left( \frac{E_a}{E_{c,\text{diff}}} \right) + 0.23 \left( \frac{E_a}{E_{c,\text{diff}}} \right)^{1/3} \right] \quad (34)$$

is the diffusion coefficient for the Kolmogorov spectrum (D. Harari et al. 2014),  $E_a$  is the energy of particle  $a$  in the lab frame,  $E_{c,\text{diff}} \approx ZeBr_{\text{ext}}$  is the critical energy, and  $r_{\text{ext}}$  denotes the typical scale of the external region, corresponding to  $r_w$  in Scenario B and  $\Delta_{\text{ext}}$  in Scenario C.

### 3. CASE STUDY: CYGNUS X-1 AND CYGNUS X-3

Recently, LHAASO reported the detection of  $\sim 100$  TeV photons from Cygnus X-1 (LHAASO Collaboration 2025a) and  $\sim$  PeV photons from Cygnus X-3 (LHAASO Collaboration 2025b). In this section, we

investigate the multimessenger emission from the microquasars Cygnus X-1 and Cygnus X-3. We select extensive multiwavelength observational data for these sources, covering energies from radio to PeV. Crucially, the observed 0.1-1 PeV photons cannot be explained by leptonic processes alone, necessitating the inclusion of hadronic processes. As described in Sect. 2, we apply three distinct scenarios with different parameter sets to fit the multiwavelength data. Our results present one plausible parameter set for each scenario that can fit the data, rather than a statistically optimized best fit.

The general properties and observational data of Cygnus X-1 and Cygnus X-3 are summarized below:

- (a) Cygnus X-1 (RA = 299.6°, DEC = 35.2°) is a high-mass X-ray binary (HMXRB) hosting a black hole with  $M_{\text{BH}} \approx 21 M_{\odot}$  in a 5.6-day orbit around an O-type donor star of  $M_{\star} \approx 41 M_{\odot}$  (J. C. A. Miller-Jones et al. 2021). Although the donor star nearly fills its Roche lobe, accretion occurs via the stellar wind (e.g., D. R. Gies et al. 2008). As shown in Figs. 4-6, we collect multiwavelength data from the literature for both the hard and soft states, incorporating observations obtained at different epochs. These include: radio to millimeter data from R. P. Fender et al. (2000); M. Pandey et al. (2006) (detected at MJD 50664-50675, 50945-50964, 52796-53392, respectively; plotted as blue points); infrared data from I. F. Mirabel et al. (1996); P. Persi et al. (1980) (MJD 43808-43827; blue points); X-ray data from M. L. McConnell et al. (2002) (pink points); 0.1-100 GeV data from *Fermi*-LAT (A. A. Zdziarski et al. 2017) (MJD 54628-57705; brown); upper limits at energies  $> 100$  MeV from AGILE (S. Saba-tini et al. 2013) (MJD 54406-55121 for hard state, and MJD 55378-55647 for soft state; purple); upper limits at energies  $> 100$  GeV from MAGIC (A. Fernandez-Barral et al. 2017) (MJD 54101-55562 for hard state; grey); and  $\gtrsim 10$  TeV data from LHAASO (LHAASO Collaboration 2025a) (MJD 58843-60340 for KM2A, and MJD 59281-60561 for WCDA; orange). For the X-ray band, we adopt the de-absorbed spectrum from A. A. Zdziarski et al. (2017) (pink solid line), corrected for absorption by the interstellar medium.
- (b) Cygnus X-3 (RA = 308.1°, DEC = 41.0°) is a wind-fed HMXRB composed of a compact object and a Wolf-Rayet companion star, with an orbital period of 4.8 hours (M. H. van Kerkwijk et al. 1992; I. I. Antokhin & A. M. Cherepashchuk 2019; I. I. Antokhin et al. 2022). While the na-

ture of the compact object remains uncertain, a black hole (BH) is favored based on extensive X-ray and radio observations (e.g., L. Hjalmarsdotter et al. 2009; A. Szostek et al. 2008; K. I. I. Koljonen & T. J. Maccarone 2017). In this work, we adopt the BH scenario, assuming a compact object mass of  $M_{\text{BH}} \approx 7 M_{\odot}$  and a total system mass of  $19 M_{\odot}$ , consistent with I. I. Antokhin et al. (2022). As shown in Figs. 4-6, we collect multiwavelength data from the literature obtained at different epochs during the soft state: radio to millimeter data from M. Pandey et al. (2006) (MJD 52797-53393; blue points); infrared data from R. N. Ogley et al. (2001) (MJD 50613-50619; blue points); X-ray data from A. Szostek et al. (2008) (pink points); 0.1-100 GeV data from *Fermi*-LAT (LHAASO Collaboration 2025b) (MJD 58848-60522; brown); upper limits at energies  $> 100$  GeV from MAGIC (J. Aleksić et al. 2010) (MJD 55033-55034; grey); and  $\gtrsim 0.1$  PeV data from LHAASO (LHAASO Collaboration 2025b) (MJD 59101-60501 for KM2A; orange). For the X-ray band, we adopt the de-absorbed spectrum from O. Vilhu et al. (2023), shown as the pink solid line. Although A. Veledina et al. (2024) reported that the intrinsic X-ray flux can be more than ten times higher than the observed flux, we use the originally observed value for a general example in our calculation.

The basic parameters of Cygnus X-1 and Cygnus X-3 are listed in Table 1. For both Cygnus X-1 and Cygnus X-3, we assume a circular orbit (eccentricity  $e = 0$ ), meaning the distance  $d$  between the donor star and the central engine is equal to the semi-major axis  $a$  at all times.

For simplicity, we adopt a fixed jet geometry for all modeling scenarios, as summarized in Table 2. Motivated by the strong stellar wind (A. Dmytriiev et al. 2024; S. Prabu et al. 2025), the jet is assumed to be deflected outward by the ram pressure of the wind, while the Coriolis force resulting from the binary’s orbital motion further bends the jet in the direction opposite to the rotation. Consequently, we set  $\Delta\phi = \phi - \phi_j = -90^\circ$  as an example. We set  $\phi = 180^\circ$  as it corresponds roughly to the mean flux during orbital modulation, which approximates the orbital-phase-averaged flux, as shown in Figs. 7 and 10. For Cygnus X-1, J. A. Tomsick et al. (2018); M. L. Parker et al. (2015) noted that the inclination inferred from the X-ray reflection spectrum,  $\sim 40^\circ$ , is not consistent with the binary inclination of  $27.1^\circ$ . Accordingly, we adopt  $\vartheta_j = 15^\circ$  for Cygnus X-1. For Cygnus X-3, modeling of the orbital modulation of gamma-ray emission indicates  $\vartheta_j \gtrsim 25^\circ$  (A. A.

Zdziarski et al. 2018; A. Dmytriiev et al. 2024), so we adopt  $\vartheta_j = 25^\circ$ . To reduce the number of free parameters, we assume a jet opening angle of  $\theta_{\text{op}} = 1/\Gamma_j$ , although the actual opening angles may be significantly smaller in these sources— $\lesssim 15^\circ$  for Cygnus X-3 (A. Veledina et al. 2024) and  $\lesssim 1^\circ$  for Cygnus X-1 (A. M. Stirling et al. 2001).

In our calculations, we adopt a total evolution time of  $10^6$  s for Scenarios A and B. While the soft state is generally less stable and shorter-lived than the hard state, and Cygnus X-1 and Cygnus X-3 exhibit different variability, this duration is justified. V. Grinberg et al. (2013) reported that Cygnus X-1 can remain in stable hard or soft states for over 300 hours, and K. I. I. Koljonen et al. (2018) observed a prolonged ( $\sim 10 - 30$  days) hypersoft state for Cygnus X-3. These timescales significantly exceed the system’s dynamical timescale for Scenarios A and B, suggesting that a steady state is achieved. Therefore, any uncertainties in the precise duration of each state should have a negligible effect on our results. For Scenario C, which represents more persistent radiation, we set the system age equal to the evolution time:  $10^6$  yr for Cygnus X-1 (J. Ziółkowski 2005) and  $10^5$  yr for Cygnus X-3 (G. Meynet & A. Maeder 2005). Again, any uncertainties in the precise age of the system should have a negligible impact on our results, as the system age is much longer than the dynamical timescale. Note that the orbital period for each source is much shorter than the evolution duration adopted in our study. For simplicity, we neglect the effects of orbital motion in our calculations.

### 3.1. Optical Depth and Production of High-Energy Photons

In our model, high-energy photons are primarily produced via the  $p\gamma$  and  $pp$  processes. Fig. 3 shows the efficiencies of  $p\gamma$  (red lines) and  $pp$  (purple lines) interactions in the blob co-moving frame for each scenario and source, illustrating the production efficiency of high-energy photons.

Within both the jet blob and the inner blob, photons above 0.1 PeV are dominated by the  $p\gamma$  process, owing to the presence of a sufficiently dense target photon field. For target photon field of  $dn_{\text{ph,t}}/dE_{\text{ph,t}} \propto E_{\text{ph,t}}^{-\alpha}$  with a spectral index  $\alpha \gtrsim 1$ , like the external seed photons from the accretion disk, the production is dominated by the  $\Delta$ -resonance. The inelasticity efficiency of the  $p\gamma$

**Table 1.** Physical parameters for Cygnus X-1 and Cygnus X-3 adopted in this work. See Tables. 2-6 for modeling parameters.

Input Parameters	Symbol [Units]	Cyg X-1 <sup>a</sup>	Cyg X-3 <sup>b</sup>
Luminosity distance	$D_L$ [kpc]	2.2	9.7
Orbital inclination	$i$ [°]	28	30
Orbital period	$P_{\text{orb}}$ [s]	$4.8 \times 10^5$	$1.7 \times 10^4$
Mass of black hole	$M_{\text{BH}}$ [ $M_\odot$ ]	21	7
Mass of donor star	$M_\star$ [ $M_\odot$ ]	41	12
Temperature of donor star	$T_\star$ [K]	$3.1 \times 10^4$	$1.0 \times 10^5$
Luminosity of donor star	$L_\star$ [erg s <sup>-1</sup> ]	$1.6 \times 10^{39}$	$7.7 \times 10^{38}$
Stellar wind mass-loss rate	$\dot{M}_w$ [ $M_\odot$ yr <sup>-1</sup> ]	$2.6 \times 10^{-6}$	$9.6 \times 10^{-6}$
Wind accel. parameter	$\beta$	1.05	2.0
Wind temperature	$T_w$ [K]	$1.0 \times 10^6$	$1.0 \times 10^6$
Derived Parameters	Symbol [Units]	Cyg X-1	Cyg X-3
Semi-major axis <sup>c</sup>	$a$ [cm]	$3.7 \times 10^{12}$	$2.7 \times 10^{11}$
Eddington luminosity	$L_{\text{Edd}}$ [erg s <sup>-1</sup> ]	$2.7 \times 10^{39}$	$9.1 \times 10^{38}$
Radius of donor star <sup>d</sup>	$R_\star$ [cm]	$1.6 \times 10^{12}$	$1.0 \times 10^{11}$
Stellar wind velocity	$v_{w,\infty}$ [cm s <sup>-1</sup> ]	$8.3 \times 10^7$	$1.7 \times 10^8$

<sup>a</sup>Parameters from J. Ziółkowski (2005); A. Szostek & A. A. Zdziarski (2007); J. C. A. Miller-Jones et al. (2021).

<sup>b</sup>Parameters from K. I. I. Koljonen & T. J. Maccarone (2017); M. J. Reid & J. C. A. Miller-Jones (2023); I. I. Antokhin et al. (2022).

<sup>c</sup>Assuming a circular orbit, the semi-major axis is given by  $a = \left( \frac{P_{\text{orb}}^2 G (M_{\text{BH}} + M_\star)}{4\pi^2} \right)^{1/3}$ .

<sup>d</sup>The stellar radius  $R_\star$  is derived from  $L_\star = 4\pi R_\star^2 \sigma_{\text{SB}} T_\star^4$ .

**Table 2.** Geometry parameters used in this work, unless otherwise specified.

Geometry Parameters	Symbol [Units]	Cygnus X-1 (hard)	Cygnus X-1 (soft)	Cygnus X-3
Jet polar angle	$\vartheta_j$ [deg]	15	15	25
Jet azimuthal angle	$\phi_j$ [deg]	-90	-90	-90
Azimuthal angle of donor star	$\phi$ [deg]	180	180	180

process can be estimated as (K. Murase et al. 2016):

$$\begin{aligned}
 f_{p\gamma} &\approx \frac{t_{\text{dyn}}}{t_{p\gamma}} \approx \eta_{p\gamma} r \beta_j^{-1} n_{\text{ph,t}} \hat{\sigma}_{p\gamma} \left( \frac{E_p}{E_{\text{ch},p\gamma}} \right)^{\alpha-1} \\
 &\simeq 8.8 \times 10^{-7} \eta_{p\gamma} r_9 \beta_{j,-0.1}^{-1} n_{\text{ph,t},13} \left( \frac{E_p}{E_{\text{ch},p\gamma}} \right)^{\alpha-1}, \quad (35)
 \end{aligned}$$

where  $\eta_{p\gamma} \approx 2/(1+\alpha)$ ,  $t_{p\gamma}$  is the timescale for a proton of energy  $E_p$  to lose energy through the  $p\gamma$  process in the lab frame,  $n_{\text{ph,t}}$  is the number density of target photons in the lab frame,  $\hat{\sigma}_{p\gamma} = \kappa_{p\gamma} \sigma_{p\gamma} \sim 0.7 \times 10^{-28}$  cm<sup>2</sup> is the product of the inelasticity and the cross section for  $p\gamma$  process,  $E_{\text{ch},p\gamma} = 0.5 \Gamma_j^2 m_p c^2 \bar{\varepsilon}_\Delta / E_{\text{ph,t}} \simeq 141$  TeV  $(E_{\text{ph,t}}/1 \text{ keV})^{-1} \Gamma_{j,0}^2$  is the characteristic proton energy with  $\bar{\varepsilon}_\Delta \sim 0.3$  GeV, and  $E_{\text{ph,t}}$  is the energy of the target photon in the observer frame. Since the external seed photons from the donor star follow a blackbody distribution (where  $\alpha < 1$ ),  $f_{p\gamma}$  becomes approximately

constant due to higher resonances and multipion production. The threshold of this efficiency at high energies can be estimated as (C. D. Dermer et al. 2014):

$$\begin{aligned}
 f_{p\gamma} &\approx \frac{t_{\text{dyn}}}{t_{p\gamma}} \approx r \beta_j^{-1} n_{\text{ph,t}} \hat{\sigma}_{p\gamma} \left[ 1 - \frac{1 + \ln y_u}{y_u} \right] \\
 &\simeq 8.8 \times 10^{-7} r_9 \beta_{j,-0.1}^{-1} n_{\text{ph,t},13} \left[ 1 - \frac{1 + \ln y_u}{y_u} \right], \quad (36)
 \end{aligned}$$

where  $y_u = (4\Gamma_j \gamma'_p E_{\text{ph,t}} / \bar{\varepsilon}_{\text{thr},p\gamma})^2$ ,  $\bar{\varepsilon}_{\text{thr},p\gamma} \simeq 400 \Gamma_j m_e c^2$ ,  $E_{\text{ph,t}} \simeq 2.82 k T_\star \simeq 24.3$  eV  $T_{\star,5}$  is the peak energy of the target photons with blackbody distribution in the observer frame, and  $\gamma'_p$  is the Lorentz factor of protons involved in  $p\gamma$  processes in the blob co-moving frame.

The typical observed photon flux produced via the  $p\gamma$  process is given by

$$E_{\text{ph}} F_{E_{\text{ph}}} \simeq \frac{1}{2} f_{p\gamma} E_p F_{E_p}, \quad (37)$$

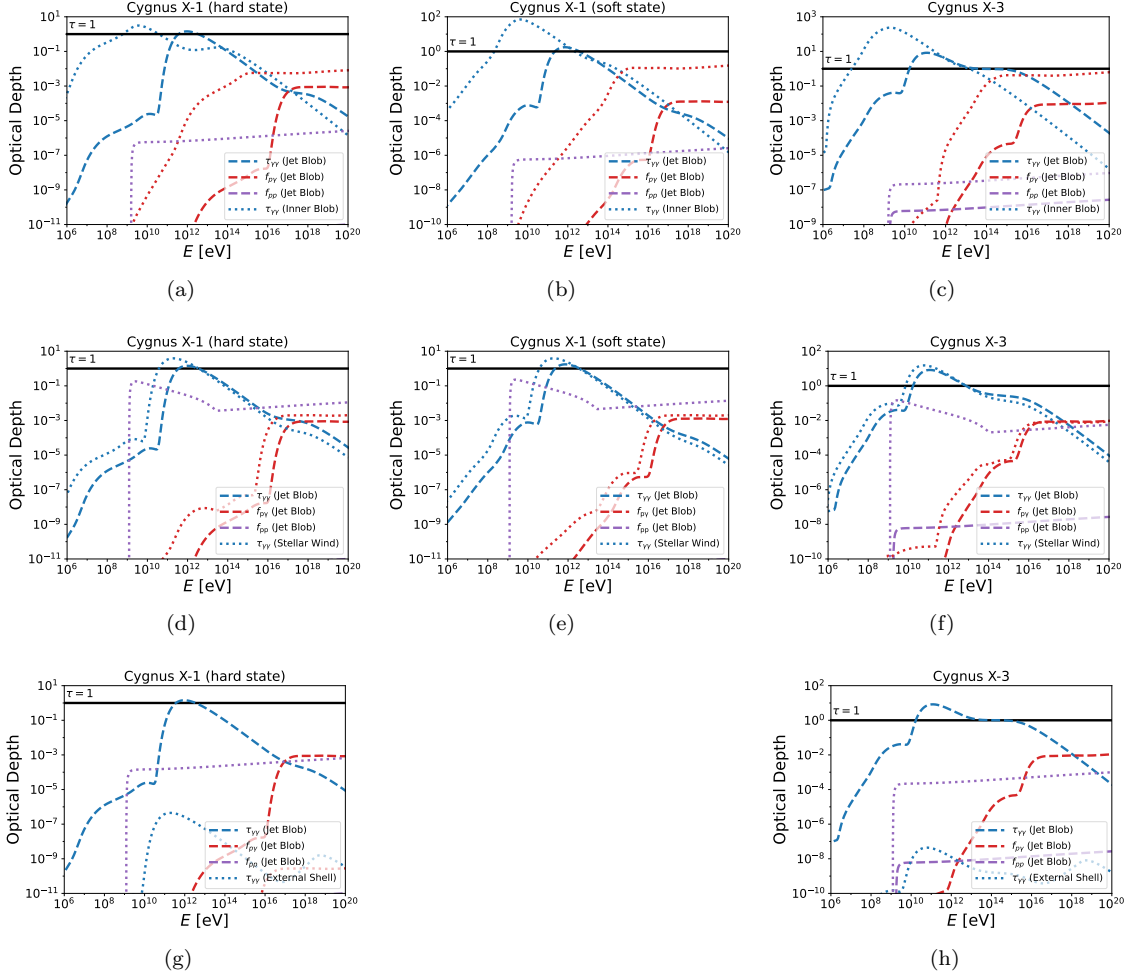


**Figure 3.** Optical depths for  $\gamma\gamma$  annihilation (blue),  $p\gamma$  interactions (red), and  $pp$  interactions (purple) in the observer frame. The first, second, and third rows correspond to Scenarios A, B, and C, respectively. Different line styles correspond to different emission zones, as indicated in the legend.

where  $E_p F_{E_p}$  is the proton flux at energy  $E_p$  in the observer frame, and the typical energy of the photon produced by a proton of energy  $E_p$  is  $E_{ph} \sim 0.1 E_p$ . Combining Eqs. 35–37, we find that the blob can generate photons with a flux of  $\sim 10^{-13}$  erg cm $^{-2}$  s $^{-1}$  around 10 TeV, given sufficient X-ray photon density, and photons with a flux of  $\sim 10^{-13}$  erg cm $^{-2}$  s $^{-1}$  around PeV, given sufficient UV photon density.

However, in  $p\gamma$  scenarios, the same photon field can also attenuate the escaping gamma-rays. The optical depth for internal  $\gamma\gamma$  annihilation can be estimated to be (e.g., K. Murase et al. 2016)

$$\begin{aligned} \tau_{\gamma\gamma} &\approx \eta_{\gamma\gamma} r \beta_j^{-1} n_{ph,t} \sigma_T \\ &\simeq 8.4 \times 10^{-3} \eta_{\gamma\gamma} r \beta_j^{-1} n_{ph,t,13}, \end{aligned} \quad (38)$$

where  $\sigma_T \approx 6.65 \times 10^{-25}$  cm $^2$  is the Thomson cross section,  $\eta_{\gamma\gamma} \approx 7/[6\alpha^{5/3}(1+\alpha)]$  for  $1 < \alpha < 7$  (R. Svensson 1987), and  $n_{ph,t}$  is the number density of target photons with energy  $E_{ph,t}$  in the observer frame.

The corresponding typical gamma-ray energy is given by  $E_{ph} \approx \Gamma_j^2 m_e^2 c^4 E_{ph,t}^{-1} \simeq 26$  GeV  $(E_{ph,t}/10$  eV) $^{-1} \Gamma_j^2$ . We find photons with energies  $\gtrsim 10$  TeV are not significantly attenuated by  $\gamma\gamma$  annihilation, where  $\tau_{\gamma\gamma} < 1$ , as indicated by the blue lines in Fig. 3.

In the external region, photons above 0.1 PeV are primarily produced via the  $pp$  process due to the dense target environment, which efficiently converts the kinetic energy of escaping protons into high-energy photons. The interaction efficiency of the  $pp$  process can be estimated as (S. R. Kelner et al. 2006; K. Murase et al. 2020):

$$\begin{aligned} f_{pp} &\approx \frac{t_{esc}}{t_{pp}} \approx c n_p \kappa_{pp} \sigma_{pp} \times \max(t_{diff}, \frac{r_{ext}}{c}), \\ &\simeq 6.0 \times 10^{-4} n_{p,9} t_{esc,3} \end{aligned} \quad (39)$$

where  $t_{pp}$  is the interaction timescale of the  $pp$  process in the lab frame,  $n_p$  is the number density of ambient protons in the lab frame,  $\kappa_{pp} \approx 0.5$  is the inelasticity

coefficient, and  $\sigma_{pp} \sim 4 \times 10^{-26} \text{ cm}^2$  is the cross section for the inelastic  $pp$  process.

The typical observed photon flux produced via the  $pp$  process is given by

$$E_{\text{ph}} F_{E_{\text{ph}}} \simeq \frac{1}{3} f_{pp} E_p F_{E_p}, \quad (40)$$

where the typical energy of a photon produced by a proton of energy  $E_p$  is  $E_{\text{ph}} \sim 0.08 E_p$ . Combining Eqs. 39–40, we find that the external region can produce photons with flux  $\sim 10^{-13} \text{ erg cm}^{-2} \text{ s}^{-1}$  at  $\sim 10 \text{ TeV}$ , and can extend up to PeV energies with flux  $\sim 10^{-14} - 10^{-15} \text{ erg cm}^{-2} \text{ s}^{-1}$ .

Both analytical estimates and numerical calculations indicate that microquasars can produce detectable photons above 0.1 PeV, even when accounting for  $\gamma\gamma$  annihilation. The  $\gamma\gamma$  absorption has a more pronounced effect in the GeV band for the inner and jet blob, where interactions with target photons are most efficient. In contrast, the influence of  $\gamma\gamma$  absorption is negligible in the external region.

### 3.2. Results for Scenario A

In Scenario A, we model the emission using a jet blob and an inner blob with parameters listed in Tables 3 and 4. Table 3 summarizes the parameters of the jet blob shared across all scenarios. For Cygnus X-1, we adopt a jet-blob height of  $10^{13} \text{ cm}$  in the lab frame, consistent with estimates based on gamma-ray modulation (R. Zanin et al. 2016). For Cygnus X-3, the corresponding height is  $3 \times 10^{11} \text{ cm}$ , in agreement with predictions from gamma-ray modulation studies (A. A. Zdziarski et al. 2018). The injected particle distributions are primarily determined by the microphysical parameters, including  $\eta_{\text{acc}}$ ,  $\epsilon_p$ ,  $\epsilon_e$ , and  $\epsilon_B$ . The maximum Lorentz factors of electrons and protons are self-consistently obtained from Eqs. 4–8.

Fig. 4 presents the resulting neutrino (black lines) and photon (red lines) spectra. The top panels show the broadband emission from radio to PeV energies, while the bottom panels focus on the gamma-ray range. In this scenario, photons above 0.1 PeV are predominantly produced via the  $p\gamma$  process, whereas GeV photons arise mainly from EIC scattering. In the energy range between 0.1 and 10 TeV, the photon spectrum exhibits a pronounced dip caused by the combined effects of the  $p\gamma$  interactions and  $\gamma\gamma$  annihilation.

The radio emission originates from synchrotron radiation but is significantly suppressed by free-free absorption. The light-red curves represent spectra without free-free absorption and external  $\gamma\gamma$  annihilation, while the red curves include these processes. The suppression of radio flux in the latter case suggests that emission

from the region located at larger heights ( $\sim 10^{14} \text{ cm}$ ; e.g., A. A. Zdziarski 2012; A. A. Zdziarski et al. 2018; A. J. Tetarenko et al. 2019), where the stellar wind density is lower, is required to reproduce the observed radio data.

#### (A) CYGNUS X-1

For Cygnus X-1, Figs. 4(a) and (d) present the model fitting results for the hard state, whereas 4(b) and (e) present the results for the soft state. The solid pink lines show the de-absorbed X-ray emission from the accretion disk, which differs between the two states. The dotted orange lines represent the blackbody radiation from the donor star, which is the same for both states. Observationally, in the soft state only upper limits are available at the GeV band, whereas in the hard state *Fermi*-LAT detected GeV photons.

For both states, the LHAASO data ( $\gtrsim 10 \text{ TeV}$ ) can be reproduced by the  $p\gamma$  process occurring in the inner blob, where the target photons originate from the X-ray radiation of the accretion disk surrounding the central engine. We also find that the inner blob can accelerate protons (electrons) up to  $\sim 100 \text{ TeV}$  ( $\sim 100 \text{ GeV}$ ).

#### (B) CYGNUS X-3

For Cygnus X-3, as shown in Figs. 4(c) and (f), our model reproduces the LHAASO data above 0.1 PeV and exhibits a two-peak structure. The first peak arises from  $p\gamma$  interactions in the inner blob, with target photons provided by the X-ray radiation of the accretion disk, while the second peak originates from  $p\gamma$  interactions in the jet blob, where the target photons come from the blackbody radiation of the donor star. Note that here we use the observed X-ray radiation without considering the possibly ten-times-larger intrinsic X-ray radiation (A. Veledina et al. 2024). This serves as a general example, and consequently, the X-ray photon density in the jet blob is insufficient to generate the required  $\sim 100 \text{ TeV}$  photons, which accounts for the difference from the modeling in LHAASO Collaboration (2025b). We find that the jet blob can accelerate protons (electrons) up to  $\sim 10 \text{ PeV}$  ( $\sim \text{TeV}$ ), whereas the inner blob can accelerate protons (electrons) up to  $\sim \text{PeV}$  ( $\sim 100 \text{ GeV}$ ).

### 3.3. Results for Scenario B

The fitting parameters for Scenario B are listed in Table 5. This scenario models a system embedded in a stellar wind environment, featuring two distinct emission regions: a primary jet blob and a static external stellar wind region. For the jet blob, we adopt the same location and radius as those used in Scenario A, while allowing some microphysical parameters to vary. The

**Table 3.** Fitting parameter values used for jet blob shared in all scenarios.

Jet Blob Parameters	Symbol [Units]	Cygnus X-1 (hard)	Cygnus X-1 (soft)	Cygnus X-3
Emission region location	$H_{\text{jet}}$ [cm]	$1.0 \times 10^{13}$	$1.0 \times 10^{13}$	$3.0 \times 10^{11}$
Emission region radius	$r_{\text{jet}}$ [cm]	$5.6 \times 10^{12}$	$7.1 \times 10^{12}$	$2.6 \times 10^{11}$
Lorentz factor (velocity)	$\Gamma_j(\beta_j)$	1.80 (0.83)	1.40 (0.70)	1.15 (0.49)
Accel. parameter	$\eta_{\text{acc}}$	$5.0 \beta_j^{-2}$	$5.0 \beta_j^{-2}$	$1.0 \beta_j^{-2}$
$p$ fraction <sup>a</sup>	$\epsilon_p$	$1.0 \times 10^{-1}$	$1.0 \times 10^{-1}$	$1.0 \times 10^{-1}$
$p$ spectral index	$s_p$	2.0	2.0	2.0
$p$ Min. Lorentz factor	$\gamma'_{p,\text{min}}$	1.0	1.0	1.0
$e^-$ spectral index	$s_e$	3.0	3.0	3.0
$e^-$ Min. Lorentz factor	$\gamma'_{e,\text{min}}$	$1.0 \times 10^2$	$1.0 \times 10^2$	$1.6 \times 10^3$
Stellar wind number density <sup>b</sup>	$n_w$ [cm <sup>-3</sup> ]	$9.8 \times 10^8$	$9.8 \times 10^8$	$2.1 \times 10^{12}$
Ambient number density <sup>c</sup>	$n'_{p,\text{jet}}$ [cm <sup>-3</sup> ]	6.6	5.5	$3.4 \times 10^5$

<sup>a</sup>We adopt jet powers of  $P_j = 0.01L_{\text{Edd}}$  for Cygnus X-1 (S. Prabu et al. 2025) and  $P_j = L_{\text{Edd}}$  for Cygnus X-3 (A. A. Zdziarski et al. 2012; A. Veledina et al. 2024), values comparable to their bolometric X-ray luminosities.

<sup>b</sup>The wind density at the center of the jet blob is given by  $n_w = \dot{M}_w / (4\pi R_{\text{jet}}^2 m_p v_w)$ , where  $R_{\text{jet}}$  is the distance between the donor star and the jet blob.

<sup>c</sup>We set the proton number density entrained in the jet to be 10% of the upper limits calculated from Eq. 12.

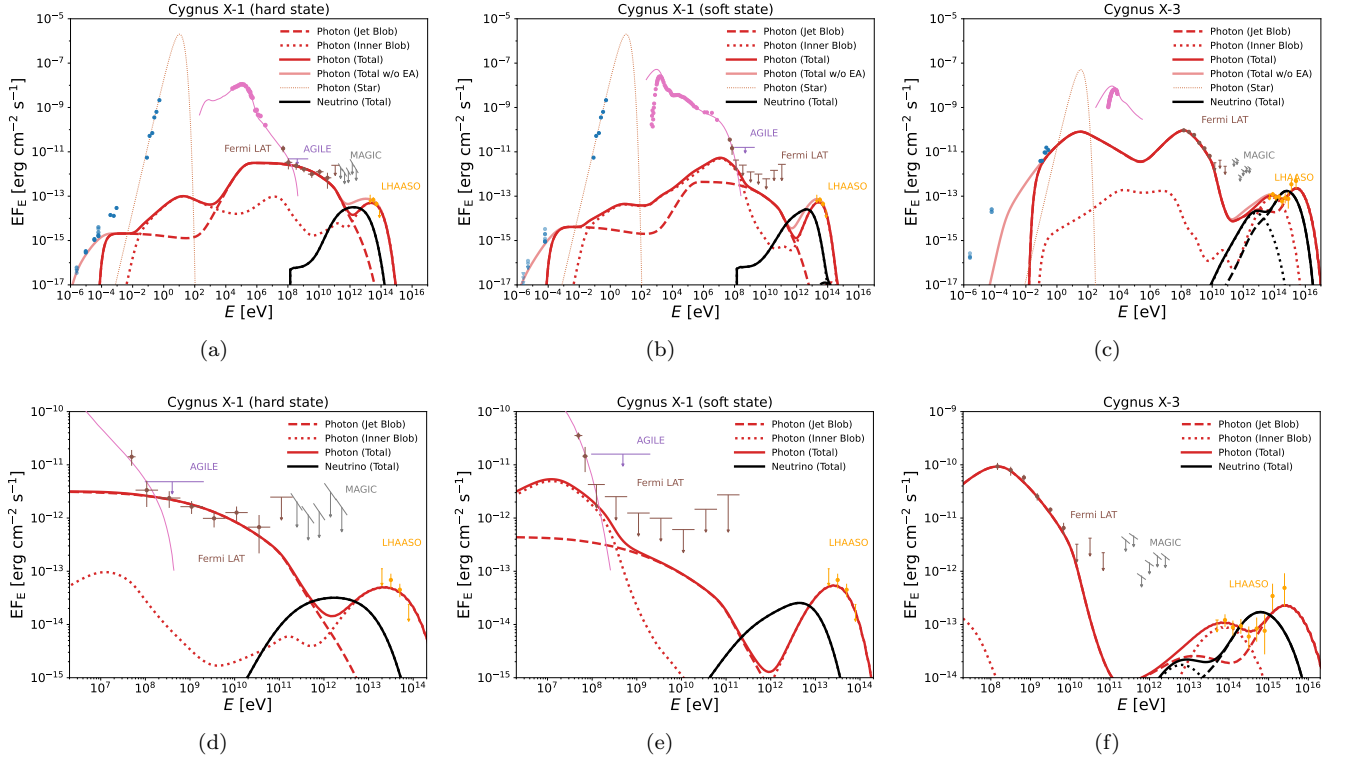


**Figure 4.** Photon (red) and neutrino (black) spectra obtained from Scenario A. The contributions to the photon and neutrino fluxes are indicated by dashed lines for the jet blob and dotted lines for the inner blob. The solid lines represent the total fluxes, summing the inner and jet blob contributions. Fainter red solid lines show photon spectra calculated without the external absorption (EA; including free-free absorption and external  $\gamma\gamma$  annihilation). Additionally, the dotted orange lines represent the blackbody radiation from the donor star, while the solid pink lines indicate the de-absorbed X-ray emission from the accretion disk. The bottom row provides a zoomed-in view of the top row. The first, second, and third columns correspond to model fits for the hard state of Cygnus X-1, the soft state of Cygnus X-1, and Cygnus X-3, respectively. Note that the observational data at different energy ranges are not simultaneous.

stellar wind region is modeled as a static spherical blob

characterized by a constant number density and mag-

**Table 4.** Fitting parameter values used for both the jet blob and the inner blob in Scenario A. Note that the remaining jet blob parameters are summarized in Table 3.

Jet Blob Parameters	Symbol [Units]	Cygnus X-1 (hard)	Cygnus X-1 (soft)	Cygnus X-3
Mag. field fraction	$\epsilon_B$	$4.0 \times 10^{-3}$	$1.0 \times 10^{-1}$	$9.0 \times 10^{-2}$
$e^-$ Fraction	$\epsilon_e$	$7.5 \times 10^{-3}$	$1.0 \times 10^{-3}$	$4.5 \times 10^{-3}$
$p$ injection luminosity	$L'_{p,\text{jet}}$ [erg s $^{-1}$ ]	$1.2 \times 10^{36}$	$1.0 \times 10^{36}$	$5.8 \times 10^{37}$
$p$ Max. Lorentz factor	$\gamma'_{p,\text{max}}$	$1.7 \times 10^5$	$6.4 \times 10^5$	$1.6 \times 10^7$
$e^-$ Max. Lorentz factor	$\gamma'_{e,\text{max}}$	$7.7 \times 10^7$	$3.1 \times 10^7$	$3.1 \times 10^6$
Inner Blob Parameters	Symbol [Units]	Cygnus X-1 (hard)	Cygnus X-1 (soft)	Cygnus X-3
Emission region location	$H_{\text{in}}$ [cm]	$1.9 \times 10^8$	$1.9 \times 10^8$	$6.4 \times 10^7$
Emission region radius <sup>a</sup>	$r_{\text{in}}$ [cm]	$1.8 \times 10^8$	$1.8 \times 10^8$	$6.1 \times 10^7$
Lorentz factor (velocity)	$\Gamma_j(\beta_j)$	1.05 (0.30)	1.05 (0.30)	1.05 (0.30)
Accel. parameter	$\eta_{\text{acc}}$	$5.0 \beta_j^{-2}$	$5.0 \beta_j^{-2}$	$1.0 \beta_j^{-2}$
Mag. field fraction <sup>b</sup>	$\epsilon_B$	$2.0 \times 10^{-2}$	$2.5 \times 10^{-3}$	$1.0 \times 10^{-3}$
$p$ fraction <sup>b</sup>	$\epsilon_p$	$1.0 \times 10^{-1}$	$1.0 \times 10^{-1}$	$3.3 \times 10^{-4}$
$e^-$ Fraction <sup>b</sup>	$\epsilon_e$	$1.0 \times 10^{-5}$	$2.0 \times 10^{-4}$	$8.1 \times 10^{-6}$
$p$ injection luminosity	$L'_{p,\text{in}}$ [erg s $^{-1}$ ]	$2.1 \times 10^{36}$	$2.1 \times 10^{36}$	$2.7 \times 10^{35}$
$p$ spectral index	$s_p$	2.0	2.0	2.0
$p$ Min. Lorentz factor	$\gamma'_{p,\text{min}}$	1.0	1.0	1.0
$p$ Max. Lorentz factor	$\gamma'_{p,\text{max}}$	$1.8 \times 10^5$	$6.4 \times 10^4$	$1.2 \times 10^6$
$e^-$ spectral index	$s_e$	3.0	3.0	3.0
$e^-$ Min. Lorentz factor	$\gamma'_{e,\text{min}}$	$1.0 \times 10^2$	$1.0 \times 10^2$	$1.6 \times 10^3$
$e^-$ Max. Lorentz factor	$\gamma'_{e,\text{max}}$	$2.0 \times 10^5$	$2.8 \times 10^5$	$1.3 \times 10^5$
Ambient number density <sup>c</sup>	$n'_{p,\text{in}}$ [cm $^{-3}$ ]	$3.2 \times 10^{10}$	$3.2 \times 10^{10}$	$3.5 \times 10^{10}$

<sup>a</sup>We adopt an inner radius of  $r_{\text{in}} = 30R_s$ , where  $R_s = GM_{\text{BH}}/c^2$  is the Schwarzschild radius of black hole.

<sup>b</sup>For simplicity, we adopt the same blob power as the jet blob:  $P_j = 0.01L_{\text{Edd}}$  for Cygnus X-1 and  $P_j = L_{\text{Edd}}$  for Cygnus X-3.

<sup>c</sup>Similar to the jet blob, we set  $n'_{p,\text{in}} = 0.1n'_{p,\text{ul}}$ .

netic field provided by the stellar wind. The wind density at the center of the jet blob, used as a reference value, is provided in Table 3.

Similar to Fig. 4, Fig. 5 presents the photon (red lines) and neutrino (black lines) spectra for Scenario B. In this scenario, photons above 0.1 PeV are primarily produced through a combination of the  $p\gamma$  process in the jet blob and the  $pp$  process in the external stellar wind region.

In the energy range between 0.1 and 10 TeV, the photon spectrum shows a mild suppression due to the combined effects of  $pp$  interactions and  $\gamma\gamma$  annihilation. As in Scenario A, GeV photons mainly originate from EIC scattering, while the radio emission is strongly attenuated by free-free absorption, implying that the observable radio emission likely arises from regions located at larger heights ( $\sim 10^{14}$  cm), where the stellar wind density is lower.

#### (A) CYGNUS X-1

For both states of Cygnus X-1, the GeV emission is attributed to the EIC process occurring in both the jet

blob and the stellar wind region, as shown in Figs. 5(a)-(b) and 5(d)-(e). The LHAASO data are well reproduced by the  $pp$  process occurring in the stellar wind region, where escaping protons interact with ambient protons in the stellar wind. Although our predicted  $\sim 80$  TeV flux slightly exceeds the 95% confidence upper limit reported by LHAASO, this discrepancy can be alleviated if the proton distribution exhibits a cutoff steeper than a simple exponential form. Such super-exponential cutoffs can naturally arise in acceleration scenarios involving magnetic reconnection (e.g., G. R. Werner et al. 2016; D. Kagan et al. 2018).

Here, we set the ambient proton number density in the stellar wind region to be around ten times larger than the value at the center of the jet blob. This density can be reduced by adopting a higher proton luminosity for the jet blob. This scenario also suggests that protons (electrons) can be accelerated up to energies of  $\sim 100$  TeV ( $\sim 10$  TeV), potentially contributing to the population of Galactic high-energy cosmic rays.

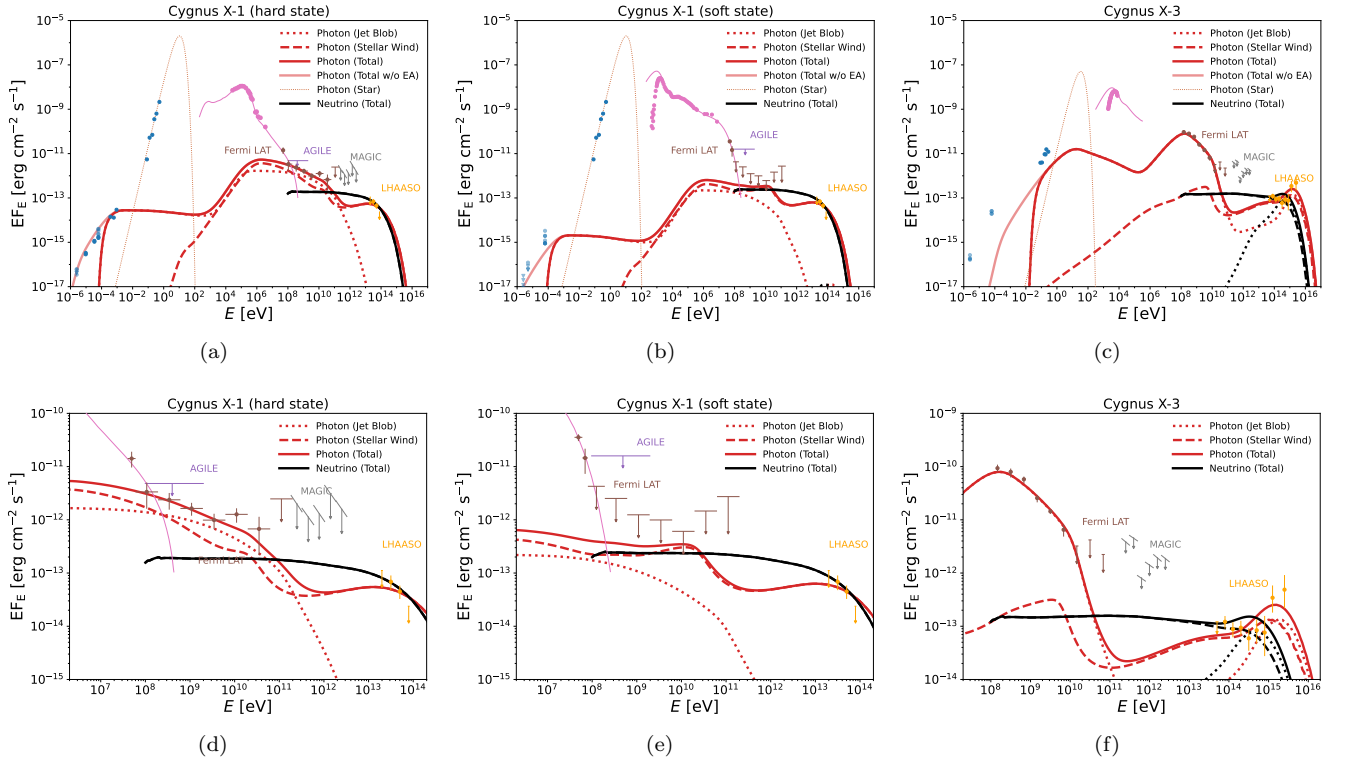
**Table 5.** Similar to Table 4, fitting parameter values used for both the jet blob and the stellar wind region in Scenario B.

Jet Blob Parameters	Symbol [Units]	Cygnus X-1 (hard)	Cygnus X-1 (soft)	Cygnus X-3
Mag. field fraction	$\epsilon_B$	$1.0 \times 10^{-1}$	$1.0 \times 10^{-1}$	$2.0 \times 10^{-2}$
$e^-$ Fraction	$\epsilon_e$	$4.0 \times 10^{-3}$	$5.0 \times 10^{-4}$	$2.5 \times 10^{-3}$
$p$ injection luminosity	$L'_{p,\text{jet}}$ [erg s $^{-1}$ ]	$1.2 \times 10^{36}$	$1.0 \times 10^{36}$	$5.8 \times 10^{37}$
$p$ Max. Lorentz factor	$\gamma'_{p,\text{max}}$	$8.4 \times 10^5$	$6.4 \times 10^5$	$7.6 \times 10^6$
$e^-$ Max. Lorentz factor	$\gamma'_{e,\text{max}}$	$3.5 \times 10^7$	$3.1 \times 10^7$	$4.5 \times 10^6$
Stellar Wind Parameters	Symbol [Units]	Cygnus X-1 (hard)	Cygnus X-1 (soft)	Cygnus X-3
Emission region Radius $^a$	$r_w$ [cm]	$1.1 \times 10^{13}$	$1.1 \times 10^{13}$	$4.0 \times 10^{11}$
Mag. field $^b$	$B_w$ [G]	$4.1 \times 10^{-2}$	$4.1 \times 10^{-2}$	4.3
$p$ escaping luminosity	$L_{p,\text{ext}}$ [erg s $^{-1}$ ]	$1.4 \times 10^{36}$	$1.5 \times 10^{36}$	$6.4 \times 10^{37}$
$e^-$ escaping luminosity	$L_{e,\text{ext}}$ [erg s $^{-1}$ ]	$5.3 \times 10^{34}$	$7.0 \times 10^{33}$	$2.3 \times 10^{30}$
Ambient number density $^c$	$n_{p,\text{ext}}$ [cm $^{-3}$ ]	$7.9 \times 10^9$	$9.8 \times 10^9$	$1.1 \times 10^{11}$

$^a$ The radius of the stellar wind region is estimated as the distance from the donor star to the center of the jet blob.

$^b$ We assume the magnetic field in the stellar wind region is given by  $B_w = \sqrt{\sigma \dot{M}_w v_w^2 / [2r_w^2 c(1 + \sigma_w)]}$ , with the magnetization parameter  $\sigma_w = 0.01$  (e.g., C. F. Kennel & F. V. Coroniti 1984; S. Shibata et al. 2003).

$^c$ We estimate the ambient proton number density contributed by the stellar wind in Scenario B.

**Figure 5.** Similar to Fig. 4, but for Scenario B. The contributions to the photon (red) and neutrino (black) fluxes are indicated by dotted lines for the jet blob and dashed lines for the stellar wind region.

### (B) CYGNUS X-3

For Cygnus X-3, as shown in Figs. 4(c) and (f), Scenario B exhibits a plateau-plus-peak structure in its emission above 10 TeV, rather than the two-peak fea-

ture seen in Scenario A. The plateau arises from  $pp$  interactions in the external blob, while the peak is produced by  $p\gamma$  interactions within the jet blob. Here, the value of  $n_{p,\text{ext}}$  in the stellar wind region is assumed to be roughly ten times lower than that at the center of

the jet blob, which can be increased if a lower proton luminosity is adopted for the jet blob. Furthermore, the overestimated flux around PeV can also be reduced with a lower proton luminosity. We adopt the current parameter values as a general example to maintain a consistent proton fraction  $\epsilon_p$  across all modelings. Similar to Scenario A, Scenario B is capable of accelerating protons (electrons) up to  $\sim 10$  PeV ( $\sim$  TeV).

### 3.4. Results for Scenario C

In Scenario C, the system is modeled with two components: an AU-scale jet blob and a parsec-scale static external shell. Within the shell, escaping particles interact with the surrounding parsec-scale medium, such as the interstellar medium or molecular clouds. The specific parameters are listed in Table 6. Phenomenologically, Scenario C is similar to Scenario B, with the key difference that the external emission originates from a large-scale shell interacting with molecular clouds rather than a stellar wind, resulting in reduced variability. To produce sufficient gamma-rays via the  $pp$  process, a dense and massive ambient medium is required. Observed giant molecular clouds in the Cygnus X region, with average densities of  $\sim 10^3$  cm $^{-3}$  and masses of  $\sim 10^5 M_\odot$ , satisfy these conditions (N. Schneider et al. 2006).

Similar to Fig. 4, Fig. 6 shows the photon (red) and neutrino (black) spectra for Scenario C. Unlike Scenario B, the external emission arises from a large-scale shell rather than a nearby stellar wind region. Consequently,  $\gamma\gamma$  annihilation is negligible, and the photon spectrum maintains a power-law shape without suppression in the 0.1-10 TeV range. Although the external shell is not affected by free-free absorption, it lacks a sufficiently strong magnetic field and a significant population of low-energy electrons, implying that the observable radio emission might still originate from regions at heights of  $\sim 10^{14}$  cm.

#### (A) CYGNUS X-1

For Cygnus X-1, we focus on modeling the hard state, as it is the most stable and commonly observed spectral state for this source (V. Grinberg et al. 2013). According to Table 6, reproducing the observed gamma-ray emission via the  $pp$  process requires a medium density of  $4.0 \times 10^2$  cm $^{-3}$  and a total mass of  $4.1 \times 10^4 M_\odot$ , consistent with the observed properties of giant molecular clouds in the Cygnus X region (N. Schneider et al. 2006). However, the value of  $n_{p,\text{ext}}$  we used is higher than the  $10$  cm $^{-3}$  used in Y. Ohira (2025). This discrepancy arises primarily because they adopted a much higher proton luminosity ( $10^{39}$  erg s $^{-1}$ ) that is inconsistent with constraints from the current kinetic instantaneous power of the jet (S. Prabu et al. 2025).

Figs. 6(a) and (c) present the resulting photon and neutrino spectra, which are similar to those in Scenario B. The LHAASO data are well reproduced by  $pp$  interactions occurring in the large-scale external shell. In this case, protons (electrons) can still be accelerated up to energies of  $\sim 100$  TeV ( $\sim 10$  TeV).

#### (B) CYGNUS X-3

For Cygnus X-3, Table 6 indicates that a dense medium with a number density of  $n_{p,\text{ext}} \simeq 2.4 \times 10^2$  cm $^{-3}$  and a total mass of  $8.4 \times 10^4 M_\odot$  is required to produce sufficient gamma-rays via the  $pp$  process, which is consistent with the observational estimates reported by N. Schneider et al. (2006).

The resulting emission in Scenario C is similar to Scenario B, as shown in Fig. 6(b) and (d). The key difference is that Scenario C exhibits a power-law plus peak structure in its emission above 10 TeV: the power-law feature originates from  $pp$  interactions in the large-scale external shell, while the peak is produced by  $p\gamma$  interactions within the jet blob. Like Scenario B, Scenario C can also accelerate protons (electrons) up to  $\sim 10$  PeV ( $\sim$  TeV).

## 4. ENERGY-DEPENDENT ORBITAL MODULATION OF GEV AND PEV EMISSION

In the previous sections, we fixed the system geometry. Here, we incorporate the effects of orbital motion to investigate the orbital modulation in the high-energy bands. Given the distant observer, we model the orbital motion as a variation in the donor star's azimuthal angle,  $\phi$ . Since the GeV and PeV emissions in all scenarios originate from the jet blob, we focus exclusively on the radiation produced by the jet blob in Cygnus X-3, adopting the same parameters as in Scenario A. It should be noted that, given the high uncertainty of the modulation model, our calculations therefore represent a plausible scenario rather than a definitive prediction.

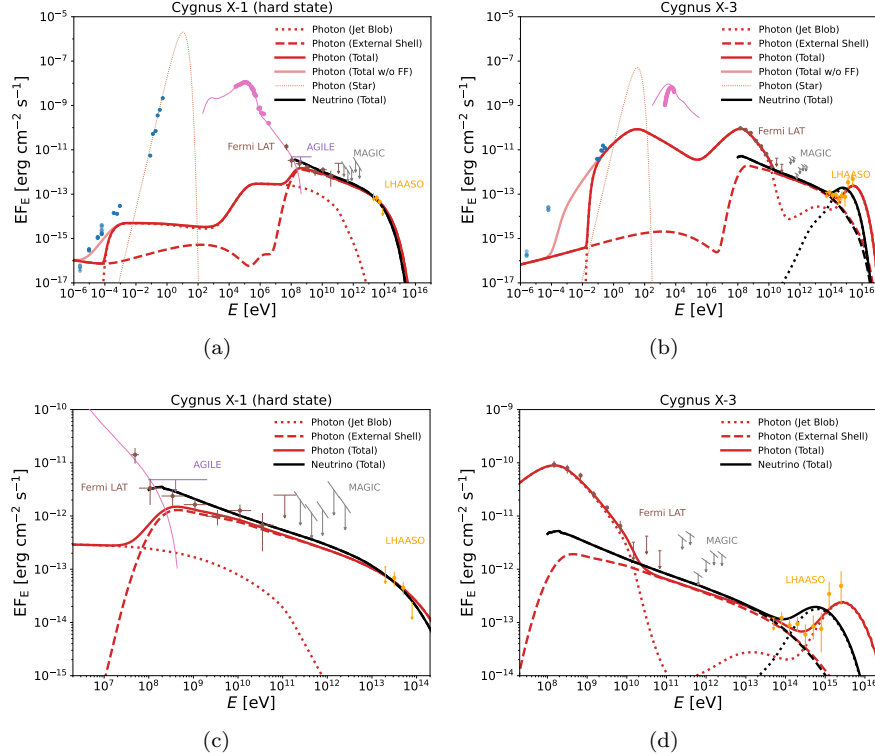
There are two primary mechanisms that can lead to orbital modulation of high-energy emission. In the first scenario, the jet orientation remains fixed relative to the observer (e.g., G. Dubus et al. 2010a; A. A. Zdziarski et al. 2018). The modulation arises from changes in the distance between the donor star and the jet blob, which alter the local photon field and consequently the emission from IC and  $p\gamma$  processes. In the second scenario, variations in the jet azimuthal angle,  $\phi_j$ , lead to changes in Doppler boosting, producing observable flux variability (e.g., G. Dubus et al. 2010b; A. Dmytriev et al. 2024). In both scenarios, strong  $\gamma\gamma$  annihilation can produce energy-dependent modulation patterns, with a more pronounced effect in the GeV band than in the PeV band due to the higher photon-photon opacity at lower

**Table 6.** Similar to Table 5, fitting parameter values used for both the jet blob and the external shell region in Scenario C.

Jet Blob Parameters	Symbol [Units]	Cygnus X-1 (hard)	Cygnus X-3
Mag. field fraction	$\epsilon_B$	$1.0 \times 10^{-1}$	$1.0 \times 10^{-1}$
$e^-$ Fraction	$\epsilon_e$	$7.0 \times 10^{-4}$	$4.5 \times 10^{-3}$
$p$ injection luminosity	$L'_{p,\text{jet}}$ [erg s $^{-1}$ ]	$1.2 \times 10^{36}$	$5.8 \times 10^{37}$
$p$ Max. Lorentz factor	$\gamma'_{p,\text{max}}$	$8.4 \times 10^5$	$1.7 \times 10^7$
$e^-$ Max. Lorentz factor	$\gamma'_{e,\text{max}}$	$3.5 \times 10^7$	$3.0 \times 10^6$
External Shell Parameters	Symbol [Units]	Cygnus X-1 (hard)	Cygnus X-3
Emission region location	$H_{\text{ext}}$ [cm]	$3.1 \times 10^{19}$	$4.6 \times 10^{19}$
Emission region width	$\Delta_{\text{ext}}$ [cm]	$1.0 \times 10^{19}$	$1.5 \times 10^{19}$
Mag. field	$B_{\text{ext}}$ [ $\mu\text{G}$ ]	10	10
$p$ escaping luminosity	$L_{p,\text{ext}}$ [erg s $^{-1}$ ]	$1.4 \times 10^{36}$	$6.4 \times 10^{37}$
$e^-$ escaping luminosity	$L_{e,\text{ext}}$ [erg s $^{-1}$ ]	$9.3 \times 10^{33}$	$1.1 \times 10^{30}$
Ambient number density $a$	$n_{p,\text{ext}}$ [cm $^{-3}$ ]	$4.0 \times 10^2$	$2.4 \times 10^2$
Total Ambient Mass $a$	$M_{p,\text{ext}}$ [ $M_\odot$ ]	$4.1 \times 10^4$	$8.4 \times 10^4$

$a$ We estimate the ambient proton number density contributed by the interstellar medium or a molecular cloud in Scenario C.

$b$ The total ambient mass is calculated as  $M_{p,\text{ext}} = V_{\text{ext}} n_{p,\text{ext}}$ , with the volume given by  $V_{\text{ext}} = 4\pi H_{\text{ext}}^2 \Delta_{\text{ext}}$ .

**Figure 6.** Similar to Fig. 4, but for Scenario C. The contributions to the photon (red) and neutrino (black) fluxes are indicated by dotted lines for the jet blob and dashed lines for the external shell.

energies. Both models have their respective advantages and limitations (A. Dmytriiev et al. 2024).

Here, we focus on the latter scenario, motivated by wind-jet interactions (S. Prabu et al. 2025). In such a

configuration, the jet is deflected outward by the ram pressure of the powerful stellar wind, while the Coriolis force induced by the binary's orbital motion further bends the jet in the direction opposite to the rotation.

For simplicity, we fix the values of  $\Delta\phi = \phi - \phi_j$  and  $\vartheta_j$  to remain constant throughout the orbital motion. In addition to the internal  $\gamma\gamma$  annihilation, which is automatically computed by AMES, we also consider external  $\gamma\gamma$  annihilation arising from photons traveling along the line-of-sight and interacting with target photon fields. The modulation arises from variations in the Doppler factor and external  $\gamma\gamma$  annihilation at different orbital phases. Notably, the maximum Doppler factor and the weakest external  $\gamma\gamma$  annihilation occur at different orbital phases, resulting in energy-dependent modulation, as shown in Fig. 7 (a).

LHAASO Collaboration (2025b) reported likely differences in the orbital modulation between the PeV, GeV, and X-ray bands as detected by LHAASO, *Fermi*-LAT, and MAXI. Specifically, the *Fermi*-LAT light curve minimum precedes that of LHAASO by approximately  $90^\circ$  in phase, while the MAXI light curve maximum lies between the minima of the LHAASO and *Fermi*-LAT data. In Fig. 7, we present the cases with  $\Delta\phi = 0^\circ, -90^\circ, \text{ and } -180^\circ$ , and  $\vartheta_j = 5^\circ, 25^\circ, \text{ and } 45^\circ$  for Cygnus X-3. Although  $\Delta\phi = 0^\circ$  is unlikely in a simple wind-jet interaction scenario assuming the average jet axis is aligned with the orbital axis, it could arise due to jet precession and/or inclination. While LHAASO collects data at  $\geq 0.1$  PeV and *Fermi*-LAT at 0.1-100 GeV, we present the predicted orbital modulation at 2 PeV, 100 GeV, and 1 GeV as illustrative examples, all dominated by jet-blob emission.

Our results indicate that if  $\gamma\gamma$  annihilation is sufficiently strong, the GeV and PeV bands may exhibit distinct modulation patterns. Furthermore, the inverse correlation between X-ray and PeV/GeV fluxes can be explained by the jet geometry. When the donor star obscures the accretion disk, thereby suppressing the X-ray flux, the jet is oriented toward the line-of-sight. This orientation maximizes the Doppler factor of the jet blob, which in turn enhances the observed PeV and GeV flux.

Within our adopted parameter set, the 1 GeV and 2 PeV emissions are unaffected by external  $\gamma\gamma$  annihilation, whereas the 100 GeV emission is strongly suppressed by it. For the case with  $\Delta\phi = -90^\circ$  and  $\vartheta_j = 25^\circ$ , the 100 GeV and 2 PeV light curves show a phase shift of approximately  $90^\circ$ , which is broadly consistent with the observational trend. However, the model faces two key challenges. First, it predicts similar behavior for the 1 GeV and 2 PeV bands, a discrepancy that calls for either stronger external annihilation or additional mechanisms. Second, while the Doppler-induced flux variation in the PeV band matches observations, the corresponding absorption-induced variation predicted at 100 GeV can exceed the observed

value by up to an order of magnitude. To align the model with GeV-band observations, additional mechanisms and more detailed treatment of external  $\gamma\gamma$  annihilation are likely required.

In this section, we propose a possible qualitative explanation for the energy-dependent modulation patterns by attributing them to variations in the Doppler factor and external  $\gamma\gamma$  annihilation. While the model captures some aspects of the observed phase differences between bands, it does not fully match the data, necessitating more detailed calculations.

## 5. PREDICTED EXPECTED NUMBER OF NEUTRINOS

In our calculations, we account for muon and pion cooling through two mechanisms: synchrotron radiation for both muons and pions, and IC scattering for muons. The inclusion of these processes, which were omitted in previous studies, reduces the predicted neutrino flux, suggesting that earlier estimates were likely overestimated.

Using the same fitting parameters listed in Tables 3-6, we find that while IC cooling of muons is negligible, synchrotron cooling of muons and pions significantly suppresses the high-energy neutrino flux. The finite lifetimes of muons and pions also contribute to this suppression. Fig. 9 shows the comparison results. Solid lines include muon and pion cooling, while dashed lines neglect these effects. The resulting suppression is significant in both the jet and inner blob, reducing the neutrino spectra by a factor of  $\sim 4$ . In the external region, these effects are minor, and the neutrino spectra remain largely unchanged due to the longer dynamical timescales and weaker magnetic fields.

Considering the muon and pion cooling effect, we calculate the expected number of neutrinos  $N_{\text{exp},\nu}$  predicted by each scenario for different detectors. The corresponding equation is given by (e.g., K. Murase & E. Waxman 2016):

$$N_{\text{exp},\nu>(> E) = \Delta t_{\text{int}} \int_E^{E_{\text{max}}} \phi_E A_{\text{eff}} dE, \quad (41)$$

where  $E$  is the energy of neutrino at observer frame,  $E_{\text{max}}$  is the energy bound for integration,  $\phi_E$  is the predicted differential neutrino flux in unit of  $\text{eV}^{-1} \text{ cm}^{-2} \text{ s}^{-1}$ ,  $A_{\text{eff}}$  is the effective area of the detector which depends on energy and the direction of the source, and  $\Delta t_{\text{int}}$  denotes the net integration time, which is less than the total observing time when accounting for the observational duty cycle. Based on archival data, Cygnus X-1 spent 75.6% (11.6%) of the time between MJD 50087 and 55200 in its hard (soft) state (V. Grinberg et al. 2013), while Cygnus X-3 was in a soft state

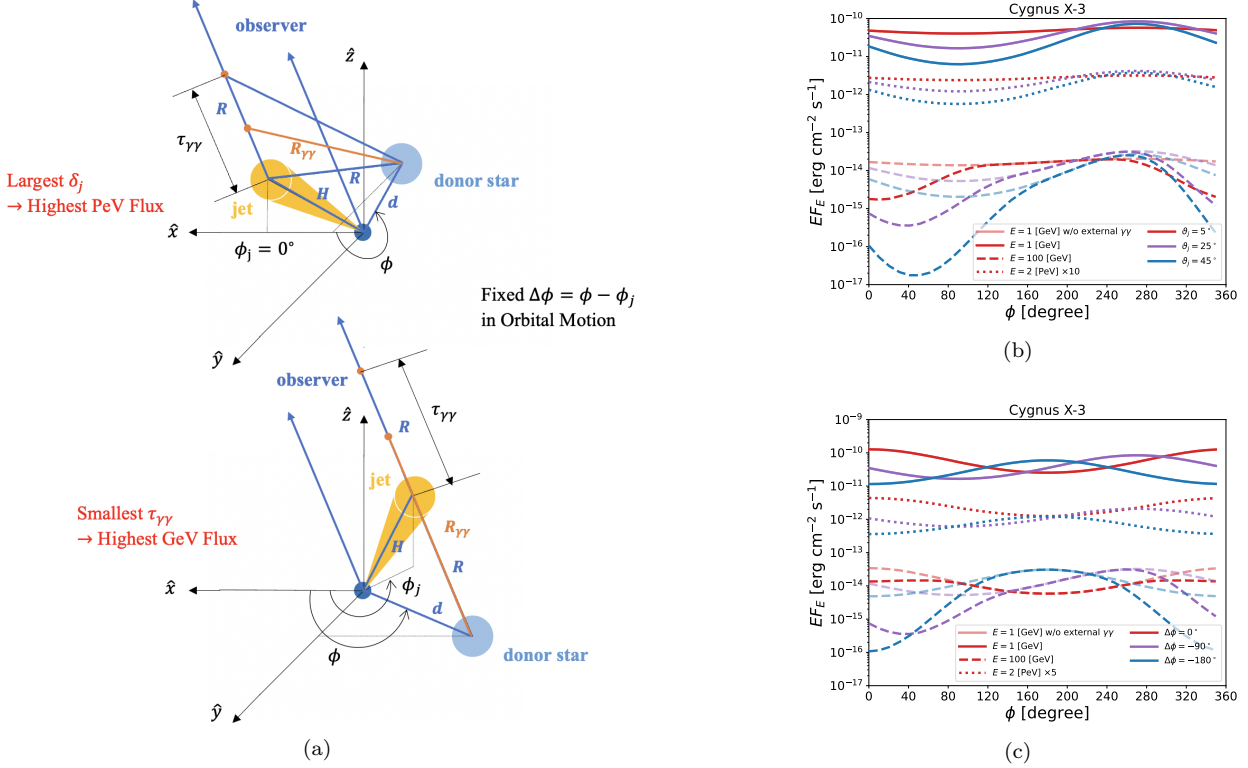


**Figure 7.** Panel (a) provides a schematic illustration of the jet blob deflection by the stellar wind, as considered in this work. The values of  $\Delta\phi$  and  $\vartheta_j$  are assumed to remain constant throughout the orbital motion. The maximum Doppler factor and the weakest external  $\gamma\gamma$  annihilation occur at different orbital phases, resulting in energy-dependent modulation. **Panels (b) and (c)** show the fluxes at selected energies for the jet blob with varying  $\vartheta_j$ ,  $\Delta\phi$ , and orbital phase  $\phi$ . For all panels, different line styles correspond to distinct energy bands. Panels (b) adopt  $\Delta\phi = -90^\circ$ , whereas Panels (c) adopt  $\vartheta_j = 25^\circ$ . In Panels (b), different colors indicate varying  $\vartheta_j$ , while in Panels (c), colors represent different  $\Delta\phi$ , as detailed in the legend. Fainter colors correspond to results calculated without external  $\gamma\gamma$  annihilation.

for 43.7% of the period between MJD 58848 and MJD 60522 (LHAASO Collaboration 2025b). Consequently, the actual observation time for each source and state can be approximated by scaling  $\Delta t_{\text{int}}$  by the inverse of these fractions: roughly  $1.3\Delta t_{\text{int}}$  ( $8.6\Delta t_{\text{int}}$ ) for Cygnus X-1 in the hard (soft) state, and  $2.3\Delta t_{\text{int}}$  for Cygnus X-3 in the soft state.

Fig. 9 shows the expected number of neutrinos detected by IceCube and IceCube-Gen2 over  $\Delta t_{\text{int}} = 20$  yr. We use the effective area  $A_{\text{eff}}$  of IceCube as provided in the all-sky point-source data from 2008 to 2018 (IceCube Collaboration et al. 2021). For IceCube-Gen2, the effective area is estimated by scaling the IceCube value by a factor of  $10^{2/3}$ , based on its approximately ten times larger detector volume (M. G. Aartsen et al. 2021). According to the model of Data-driven muon-calibrated neutrino flux (DDM) (J. P. Yañez & A. Fedynitch 2023), we calculate the expected number of atmospheric neutrino background, which is shown as the red solid lines in Fig. 9. Note that the angular window for the background is determined using the equation  $\Delta\Omega = \pi \max(\theta_{\text{res}}^2, \theta_k^2)$ , where the angular resolution is taken as  $\theta_{\text{res}} = 0.5^\circ$

( $0.1^\circ$ ) for IceCube (IceCube-Gen2), and the kinematic angle is approximated as  $\theta_k \simeq 1.5^\circ (E/1 \text{ TeV})^{-1/2}$  (K. Murase et al. 2013).

Fig. 9 presents results for three scenarios, using different colors to denote each one (blue for Scenario A, purple for Scenario B, brown for Scenario C). For a source to be considered detected, the expected number of source neutrinos,  $N_{\text{exp},\nu}$ , must exceed both the expected atmospheric background and a threshold value, typically taken as  $N_{\text{thr}} = 1$ . We find that it is almost impossible for IceCube and IceCube-Gen2 to detect neutrinos from Cygnus X-1 with  $\Delta t_{\text{int}} = 20$  yr, as the signal is entirely obscured by atmospheric neutrinos. Although the expected number of neutrinos from Cygnus X-3 detected by IceCube-Gen2 can exceed the atmospheric neutrino background at around 100 TeV, the limited number of expected neutrino detections makes a statistically significant detection challenging. Moreover, accounting for the duty cycle, the required observation time for Cygnus X-3 extends to approximately 46 years.

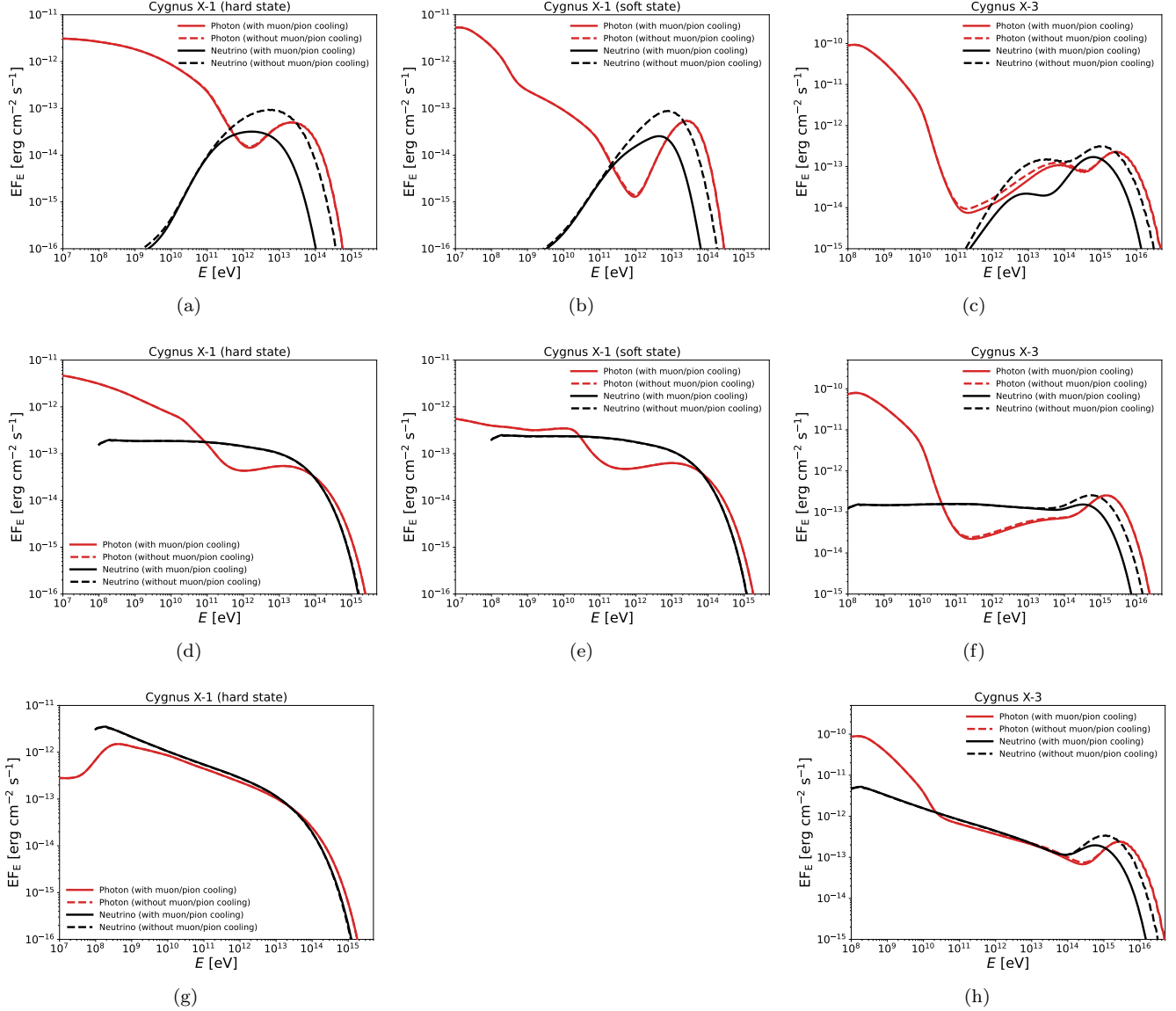


**Figure 8.** Photon (red) and neutrino (black) spectra are shown for Scenarios A (first row), B (second row), and C (third row). Solid lines represent results including the effects of muon and pion cooling, whereas dashed lines show results without these cooling processes.

## 6. SUMMARY AND DISCUSSION

In this work, we utilized AMES to investigate multimessenger emission from microquasars. Motivated by recent LHAASO detections of photons above 0.1 PeV from Cygnus X-1 and Cygnus X-3 (LHAASO Collaboration 2025a,b), we modeled their multiwavelength emission from radio to PeV energies with three distinct physical scenarios. Scenario A represents the jet-core model, comprising a jet blob produced by the terminal shock or internal shocks, and an inner blob originating from the corona or internal shocks in the compact outflow. In contrast, Scenarios B and C consist of a primary jet blob as well as a static stellar wind region or large-scale

external shell, within which escaping charged particles interact with the surrounding environment.

We found that the multiwavelength data for both Cygnus X-1 and Cygnus X-3 could be successfully reproduced in all scenarios, except for the radio band, which can be suppressed by free-free absorption, indicating that the radio-emitting region lies at larger heights ( $\sim 10^{14}$  cm). For Cygnus X-1, we adopted a lower Lorentz factor and particle injection luminosity in the soft state compared to the hard state, consistent with theoretical expectations. For Cygnus X-3, which is more distant, we also adopted a relatively low Lorentz factor for the soft state. A larger jet polar angle was required

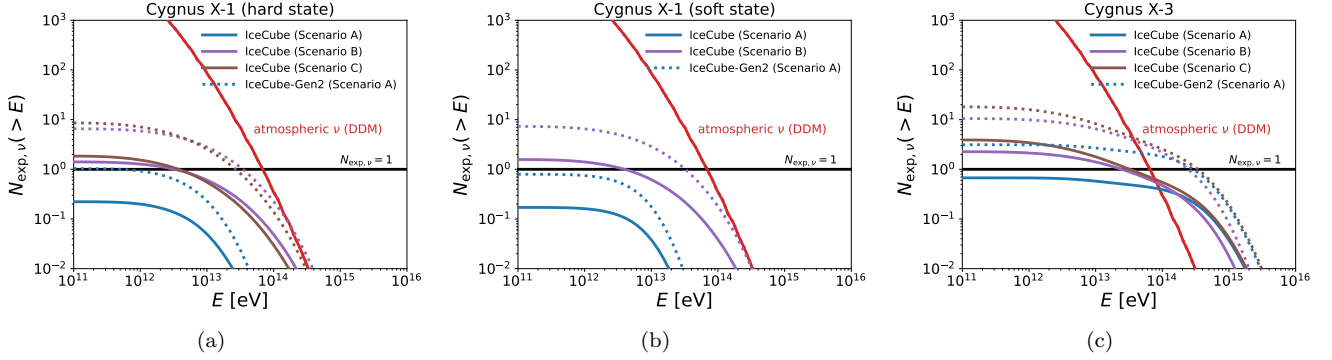


**Figure 9.** Expected number for neutrino with  $\Delta t_{\text{int}} = 20$  yr. Colors represent different scenarios, as indicated in the legend. Solid lines indicate the expected number for IceCube, while dotted lines show the expectation for IceCube-Gen2. The solid red line displays the predicted atmospheric neutrino background derived from DDM. A black parallel line serves as a reference at an expected number value of 1.

to fit the data of Cygnus X-3, implying a more inclined jet orientation.

Our modeling further provided insights into the particle acceleration mechanism, characterized by the acceleration parameter  $\eta_{\text{acc}}$ , which sets the maximum proton Lorentz factor  $\gamma'_{p, \text{max}}$ . For Cygnus X-3 (Cygnus X-1), we found  $\eta_{\text{acc}} = 1.0 \beta_j^{-2}$  ( $5.0 \beta_j^{-2}$ ). The weaker ability of Cygnus X-1 to accelerate protons to PeV energies prevented it from generating photons above 0.1 PeV, in contrast to Cygnus X-3. These values constrained the acceleration mechanism and underscored the need for further investigation. In contrast, leptonic processes, such as inverse Compton scattering from energetic electrons, could not explain the PeV data: the maximum electron energy, limited by cooling effects, was below 0.1 PeV, insufficient to produce PeV photons.

In all scenarios, the GeV emission from Cygnus X-3 is dominated by leptonic processes within the jet blob. For Cygnus X-1, the dominant mechanism varies: in Scenario A, GeV emission is dominated by leptonic processes in the jet blob; in Scenario B, it receives contributions from leptonic processes in both radiation zones; and in Scenario C, it is dominated by hadronic processes in the external region. However, at lower energies ( $E \lesssim 100$  GeV), the emission does not exhibit sufficiently distinct behavior to differentiate between these scenarios.

The model predictions for different scenarios began to diverge at higher energies. For Cygnus X-1, the TeV gamma-ray data were explained either by the  $p\gamma$  process in the inner blob (Scenario A), where the target photons originate from the X-ray radiation of the accretion disk, or by the  $pp$  process in the external region (Scenarios B and C). For Cygnus X-3, which exhibited a two-peak structure in Scenario A or a plateau (power-law) plus peak structure in Scenarios B (C), our models

attributed the first peak or plateau/power-law to the  $p\gamma$  process in the inner blob (Scenario A) with target photons from the accretion disk, or to the  $pp$  process in the external region (Scenarios B and C). The second, higher-energy peak was attributed to  $p\gamma$  interactions occurring in the jet blob in all scenarios, with target photons originating from the blackbody radiation of the donor star. This may provide another explanation for the absence of a PeV feature in Cygnus X-1. Except for the smaller  $\gamma'_{p, \text{max}}$ , the lack of a signal was likely due to the lower target photon density, which results from the wider binary separation in this system. However, PeV photon production in Cygnus X-1 cannot be ruled out if the power of its central engine were to increase.

Although all scenarios successfully reproduced the current data, they differed in their predictions at other energies, particularly in the 0.1 – 10 TeV energy band, where only upper limits are currently available. Scenario A predicted a deep dip, Scenario B a mild suppression, and Scenario C a featureless power-law spectrum. Additional observations in this range are crucial for distinguishing between the possible emission origins. Future instruments like the Cherenkov Telescope Array (CTA) will be pivotal, as its expected sensitivity of  $10^{-13}$ – $10^{-14}$  erg cm $^{-2}$  s $^{-1}$  in the 0.1–100 TeV range for a 50-hour exposure (B. S. Acharya et al. 2013) is well-suited to detect the subtle spectral features predicted by our models.

Furthermore, around 10 TeV for Cygnus X-1 and Cygnus X-3, different emission mechanisms dominate in Scenarios A, B, and C, offering a potential means to distinguish between these scenarios through future variability observations. Scenario A was expected to produce strong flux variability, whereas Scenarios B and C were predicted to exhibit weaker variability because their emission originates from larger spatial regions. In Sce-

nario A, the emission arises from the inner blob, characterized by short dynamical timescales of  $10^{-3}$ - $10^{-2}$  s, leading to rapid variations. In Scenario B, the emission originates from the external stellar wind region with dynamical timescales of  $10$ - $10^2$  s, which are much shorter than the typical durations of either the hard or soft states, as well as the orbital period. This could result in modest fluctuations in the gamma-ray flux. Scenario C, in contrast, involves large-scale external regions with a dynamical timescale of  $\sim 10^8$  s, which greatly exceeds both the orbital and state timescales, producing nearly steady, persistent emission.

We also investigated how the jet geometry, characterized by the azimuthal angle of the jet ( $\phi_j$ ) and the polar angle ( $\vartheta_j$ ), influences the predicted electromagnetic emission over the orbital phase ( $\phi$ ). Given the high uncertainty of the modulation model, our calculations presented one plausible scenario rather than a definitive prediction. This analysis assumed a fixed relative orientation  $\Delta\phi = \phi - \phi_j$  and focuses on the jet blob, as both the GeV and PeV photons originate from this region. A more detailed analysis, including the TeV photon contribution from the inner blob, was provided in the appendix. Our results indicated that sufficiently strong external  $\gamma\gamma$  absorption could induce distinct orbital modulation patterns between the GeV and PeV bands, depending on the source geometry. Furthermore, the nearly inverse modulation between the PeV and X-ray bands could be consistently caused by the jet geometry coupled with the periodic obscuration of the X-ray source by the donor star.

LHAASO Collaboration (2025b) reported likely differences in the orbital modulation between the PeV, GeV, and X-ray bands. A model with  $\Delta\phi \approx -90^\circ$  (consistent with a wind-jet interaction scenario) could reproduce the observed  $\sim 90^\circ$  phase shift between 100 GeV and 2 PeV photons. However, the model faced two key challenges: (1) it predicted similar 1 GeV and 2 PeV light curves, requiring either stronger external annihilation or additional mechanisms, and (2) while matching the observed PeV flux variation from Doppler boosting,

it overpredicted the 100 GeV variation from external  $\gamma\gamma$  annihilation by up to an order of magnitude. This work presented a simplified model where modulation arises solely from variations in Doppler boosting and external  $\gamma\gamma$  absorption. Consequently, a more detailed treatment is needed for future work.

Finally, we calculated the expected neutrino event counts for all scenarios using current and next-generation detectors. Our results accounted for muon and pion cooling, which suppresses the neutrino flux and reduces detectability. This effect was not considered in previous studies, indicating that their predictions may have been biased toward higher values. For Cygnus X-1, our models predicted that detection with IceCube or IceCube-Gen2 within  $\Delta t_{\text{int}} = 20$  yr is highly unlikely, as the predicted signal remained well below the atmospheric neutrino background. The prospects for Cygnus X-3 were slightly more promising: for IceCube-Gen2 and given an observation time of approximately 46 yr, the predicted neutrino flux could exceed the atmospheric background in a narrow energy window around 100 TeV. However, the relatively small number of expected neutrino detections associated with this excess made a statistically significant detection challenging. These findings underscored that discovering neutrino emission from microquasars will likely require a future generation of more sensitive detectors.

## ACKNOWLEDGMENTS

We thank Abraham Falcone, Derek Fox, David Radice, and Stephanie Wissel for their valuable suggestions, and Abhishek Das and Mainak Mukhopadhyay for their helpful support. The work of K.M. was supported by the NSF Grants No. AST-2108466, No. AST-2108467, and No. 2308021, and KAKENHI No. 20H05852. B.T.Z. is supported in China by National Key R&D program of China under the grant 2024YFA1611402.

## APPENDIX

### A. INFLUENCE OF GEOMETRY ON OBSERVED ELECTROMAGNETIC SIGNALS

Here, we further investigate the influence of the system geometry, characterized by the angles  $\phi$ ,  $\phi_j$ , and  $\vartheta_j$ , on the observed electromagnetic emission. As in Sect. 4, we assume the phase offset  $\Delta\phi = \phi - \phi_j$  remains fixed throughout the orbital motion. This is motivated by the wind-jet interaction model, where flux variations arise primarily from changes in the Doppler factor and external  $\gamma\gamma$  absorption. Our analysis is restricted to Scenario A, as the external emission regions in Scenarios B and C are static and more distant from the central engine, making their observed

radiation less sensitive to geometric changes. It is noted that the calculations presented here outline one plausible scenario rather than a definitive prediction.

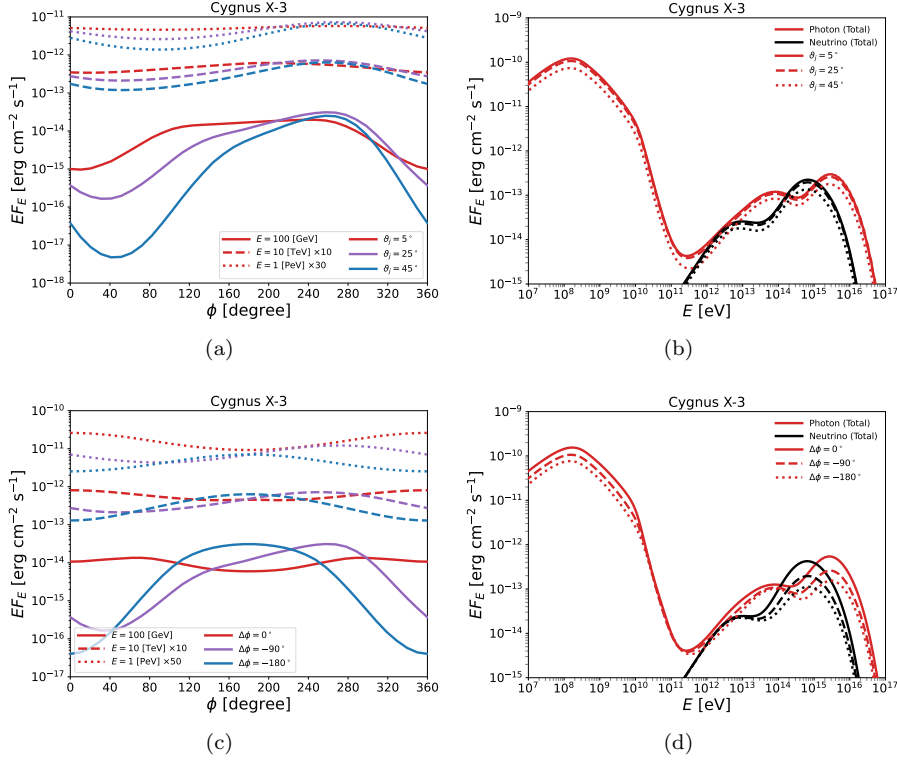


**Figure 10.** Orbital modulation for Cygnus X-3 derived from Scenario A, shown for varied jet geometry parameters  $\vartheta_j$  and  $\Delta\phi$ . The first row shows results for different jet polar angles  $\vartheta_j$  with a fixed phase offset of  $\Delta\phi = -90^\circ$ . The second row shows results for different phase offsets  $\Delta\phi$  with a fixed jet polar angle of  $\vartheta_j = 25^\circ$ . The first column displays the flux as a function of orbital phase for three energy bands: 100 GeV, 10 TeV, and 1 PeV, denoted by different line styles. The second column shows the orbital-phase-averaged photon (red) and neutrino (black) spectra.

We use Cygnus X-3 as an example to illustrate these effects. In Fig. 10, we systematically vary the geometric angles  $\phi$ ,  $\Delta\phi$ , and  $\vartheta_j$  for the inner and jet blobs while keeping all other physical parameters fixed to the values in Tables 3 and 4, focusing on high-energy photon behavior ( $> 1$  GeV). We find different choices of  $\Delta\phi$  and  $\vartheta_j$  can lead to flux differences of up to an order of magnitude. Furthermore, different energy bands exhibit distinct behaviors due to varying levels of external  $\gamma\gamma$  absorption and different dominant emission regions (jet blob versus inner blob).

The first column shows the flux as a function of orbital phase  $\phi$  for different energy bands, assuming fixed values of  $\vartheta_j$  and  $\Delta\phi$ . We find that larger values of  $\vartheta_j$  produce stronger modulation. For different  $\Delta\phi$ , the orbital modulation pattern also changes across energy bands due to the energy-dependent nature of external  $\gamma\gamma$  absorption. The second column presents the phase-averaged flux over a full orbital period ( $\phi = 0$  to  $2\pi$ ), supporting the same conclusions mentioned above.

In our models, photons from 1 to 100 TeV originate from different regions, including the inner blob, the stellar wind region, and the large-scale external region, depending on the scenario. In Scenario A, 10 TeV photons exhibit orbital modulation whose phase relationship to the 100 GeV and PeV bands (e.g., opposite, shifted, or in-phase) depends on the geometry, primarily due to strong external  $\gamma\gamma$  absorption. If 10 TeV photons are produced within the jet blob under the assumption of an intrinsic X-ray luminosity ten times larger, their behavior will become similar to that at PeV energies, offering a potential observational discriminant between the models. In contrast, Scenarios B and C are expected to show weaker orbital modulation, as their emission arises from more extended, static regions that are less affected by orbital motion. Future observations of high-energy gamma-ray modulation will therefore be critical for constraining the jet geometry and identifying the dominant radiation mechanisms.

Our results demonstrate that the combined effects of a variable Doppler factor and external  $\gamma\gamma$  absorption are sufficient to generate pronounced orbital modulation, highlighting the importance of its detailed study. However, our calculations do not include anisotropic processes, which are expected to introduce significant orbital modulation across wavelengths from radio to PeV. Furthermore, we assume a circular orbit ( $e = 0$ ), and the modulation could be even more pronounced in an elliptical orbit. Therefore, a more comprehensive treatment remains to be developed in future work.

## REFERENCES

- Aartsen, M. G., Abbasi, R., Ackermann, M., et al. 2021, *Journal of Physics G Nuclear Physics*, 48, 060501, doi: [10.1088/1361-6471/abbd48](https://doi.org/10.1088/1361-6471/abbd48)
- Abeysekera, A. U., Albert, A., Alfaro, R., et al. 2018, *Nature*, 562, 82, doi: [10.1038/s41586-018-0565-5](https://doi.org/10.1038/s41586-018-0565-5)
- Acharya, B. S., Actis, M., Aghajani, T., et al. 2013, *Astroparticle Physics*, 43, 3, doi: [10.1016/j.astropartphys.2013.01.007](https://doi.org/10.1016/j.astropartphys.2013.01.007)
- Acharyya, A., Aharonian, F., Ashkar, H., et al. 2025, arXiv e-prints, arXiv:2511.10537, doi: [10.48550/arXiv.2511.10537](https://doi.org/10.48550/arXiv.2511.10537)
- Aleksić, J., Antonelli, L. A., Antoranz, P., et al. 2010, *ApJ*, 721, 843, doi: [10.1088/0004-637X/721/1/843](https://doi.org/10.1088/0004-637X/721/1/843)
- Alfaro, R., Alvarez, C., Arteaga-Velázquez, J. C., et al. 2024, *Nature*, 634, 557, doi: [10.1038/s41586-024-07995-9](https://doi.org/10.1038/s41586-024-07995-9)
- Antokhin, I. I., & Cherepashchuk, A. M. 2019, *ApJ*, 871, 244, doi: [10.3847/1538-4357/aafb38](https://doi.org/10.3847/1538-4357/aafb38)
- Antokhin, I. I., Cherepashchuk, A. M., Antokhina, E. A., & Tatarnikov, A. M. 2022, *ApJ*, 926, 123, doi: [10.3847/1538-4357/ac4047](https://doi.org/10.3847/1538-4357/ac4047)
- Baerwald, P., & Guetta, D. 2013, *ApJ*, 773, 159, doi: [10.1088/0004-637X/773/2/159](https://doi.org/10.1088/0004-637X/773/2/159)
- Bednarek, W. 2005, *ApJ*, 631, 466, doi: [10.1086/432411](https://doi.org/10.1086/432411)
- Blumenthal, G. R., & Gould, R. J. 1970, *Reviews of Modern Physics*, 42, 237, doi: [10.1103/RevModPhys.42.237](https://doi.org/10.1103/RevModPhys.42.237)
- Carpio, J., Kheirandish, A., & Zhang, B. 2025, arXiv e-prints, arXiv:2506.22550, doi: [10.48550/arXiv.2506.22550](https://doi.org/10.48550/arXiv.2506.22550)
- Cooper, A. J., Gaggero, D., Markoff, S., & Zhang, S. 2020, *MNRAS*, 493, 3212, doi: [10.1093/mnras/staa373](https://doi.org/10.1093/mnras/staa373)
- Dermer, C. D., Murase, K., & Inoue, Y. 2014, *Journal of High Energy Astrophysics*, 3, 29, doi: [10.1016/j.jheap.2014.09.001](https://doi.org/10.1016/j.jheap.2014.09.001)
- Distefano, C., Guetta, D., Waxman, E., & Levinson, A. 2002, *ApJ*, 575, 378, doi: [10.1086/341144](https://doi.org/10.1086/341144)
- Dmytriiev, A., Zdziarski, A. A., Malyshev, D., Bosch-Ramon, V., & Chernyakova, M. 2024, *ApJ*, 972, 85, doi: [10.3847/1538-4357/ad6440](https://doi.org/10.3847/1538-4357/ad6440)
- Done, C., Gierliński, M., & Kubota, A. 2007, *A&A Rv*, 15, 1, doi: [10.1007/s00159-007-0006-1](https://doi.org/10.1007/s00159-007-0006-1)
- Dubus, G., Cerutti, B., & Henri, G. 2010a, *MNRAS*, 404, L55, doi: [10.1111/j.1745-3933.2010.00834.x](https://doi.org/10.1111/j.1745-3933.2010.00834.x)
- Dubus, G., Cerutti, B., & Henri, G. 2010b, *A&A*, 516, A18, doi: [10.1051/0004-6361/201014023](https://doi.org/10.1051/0004-6361/201014023)
- Fang, K., Halzen, F., Heinz, S., & Gallagher, J. S. 2024, *ApJL*, 975, L35, doi: [10.3847/2041-8213/ad887b](https://doi.org/10.3847/2041-8213/ad887b)
- Fender, R. 2001, in *American Institute of Physics Conference Series*, Vol. 558, High Energy Gamma-Ray Astronomy: International Symposium, ed. F. A. Aharonian & H. J. Völk (AIP), 221–233, doi: [10.1063/1.1370793](https://doi.org/10.1063/1.1370793)
- Fender, R. 2006, in *Compact stellar X-ray sources*, ed. W. H. G. Lewin & M. van der Klis, Vol. 39, 381–419, doi: [10.48550/arXiv.astro-ph/0303339](https://doi.org/10.48550/arXiv.astro-ph/0303339)
- Fender, R. P., Gallo, E., & Jonker, P. G. 2003, *MNRAS*, 343, L99, doi: [10.1046/j.1365-8711.2003.06950.x](https://doi.org/10.1046/j.1365-8711.2003.06950.x)
- Fender, R. P., Pooley, G. G., Durouchoux, P., Tilanus, R. P. J., & Brocksopp, C. 2000, *MNRAS*, 312, 853, doi: [10.1046/j.1365-8711.2000.03219.x](https://doi.org/10.1046/j.1365-8711.2000.03219.x)
- Fernandez-Barral, A., Blanch, O., de Oña Wilhemi, E., et al. 2017, in *International Cosmic Ray Conference*, Vol. 301, 35th International Cosmic Ray Conference (ICRC2017), 734, doi: [10.22323/1.301.0734](https://doi.org/10.22323/1.301.0734)
- Gaisser, T. K., & Stanev, T. 1985, *PhRvL*, 54, 2265, doi: [10.1103/PhysRevLett.54.2265](https://doi.org/10.1103/PhysRevLett.54.2265)
- Gies, D. R., Bolton, C. T., Blake, R. M., et al. 2008, *ApJ*, 678, 1237, doi: [10.1086/586690](https://doi.org/10.1086/586690)
- Gould, R. J., & Schröder, G. P. 1967, *Physical Review*, 155, 1404, doi: [10.1103/PhysRev.155.1404](https://doi.org/10.1103/PhysRev.155.1404)
- Grinberg, V., Hell, N., Pottschmidt, K., et al. 2013, *A&A*, 554, A88, doi: [10.1051/0004-6361/201321128](https://doi.org/10.1051/0004-6361/201321128)
- Harari, D., Mollerach, S., & Roulet, E. 2014, *PhRvD*, 89, 123001, doi: [10.1103/PhysRevD.89.123001](https://doi.org/10.1103/PhysRevD.89.123001)
- Hjalmarsdotter, L., Zdziarski, A. A., Szostek, A., & Hannikainen, D. C. 2009, *MNRAS*, 392, 251, doi: [10.1111/j.1365-2966.2008.14036.x](https://doi.org/10.1111/j.1365-2966.2008.14036.x)
- IceCube Collaboration, Abbasi, R., Ackermann, M., et al. 2021, arXiv e-prints, arXiv:2101.09836, doi: [10.48550/arXiv.2101.09836](https://doi.org/10.48550/arXiv.2101.09836)
- Kachelrieß, M., & Lammert, E. 2025, *A&A*, 701, A22, doi: [10.1051/0004-6361/202554701](https://doi.org/10.1051/0004-6361/202554701)

- Kagan, D., Nakar, E., & Piran, T. 2018, *MNRAS*, 476, 3902, doi: [10.1093/mnras/sty452](https://doi.org/10.1093/mnras/sty452)
- Kantzas, D., Markoff, S., Beuchert, T., et al. 2021, *MNRAS*, 500, 2112, doi: [10.1093/mnras/staa3349](https://doi.org/10.1093/mnras/staa3349)
- Kelner, S. R., Aharonian, F. A., & Bugayov, V. V. 2006, *PhRvD*, 74, 034018, doi: [10.1103/PhysRevD.74.034018](https://doi.org/10.1103/PhysRevD.74.034018)
- Kennel, C. F., & Coroniti, F. V. 1984, *ApJ*, 283, 710, doi: [10.1086/162357](https://doi.org/10.1086/162357)
- Kimura, S. S., Murase, K., & Mészáros, P. 2020, *ApJ*, 904, 188, doi: [10.3847/1538-4357/abbe00](https://doi.org/10.3847/1538-4357/abbe00)
- Koljonen, K. I. I., Maccarone, T., McCollough, M. L., et al. 2018, *A&A*, 612, A27, doi: [10.1051/0004-6361/201732284](https://doi.org/10.1051/0004-6361/201732284)
- Koljonen, K. I. I., & Maccarone, T. J. 2017, *MNRAS*, 472, 2181, doi: [10.1093/mnras/stx2106](https://doi.org/10.1093/mnras/stx2106)
- Kuze, R., Kimura, S. S., & Fang, K. 2025, *ApJ*, 985, 139, doi: [10.3847/1538-4357/adcc1b](https://doi.org/10.3847/1538-4357/adcc1b)
- Levinson, A., & Waxman, E. 2001, *PhRvL*, 87, 171101, doi: [10.1103/PhysRevLett.87.171101](https://doi.org/10.1103/PhysRevLett.87.171101)
- LHAASO Collaboration. 2025a, *National Science Review*, nwaf496, doi: [10.1093/nsr/nwaf496](https://doi.org/10.1093/nsr/nwaf496)
- LHAASO Collaboration. 2025b, *arXiv e-prints*, arXiv:2512.16638, doi: [10.48550/arXiv.2512.16638](https://doi.org/10.48550/arXiv.2512.16638)
- McConnell, M. L., Zdziarski, A. A., Bennett, K., et al. 2002, *ApJ*, 572, 984, doi: [10.1086/340436](https://doi.org/10.1086/340436)
- Meynet, G., & Maeder, A. 2005, *A&A*, 429, 581, doi: [10.1051/0004-6361:20047106](https://doi.org/10.1051/0004-6361:20047106)
- Miller-Jones, J. C. A., Bahramian, A., Orosz, J. A., et al. 2021, *Science*, 371, 1046, doi: [10.1126/science.abb3363](https://doi.org/10.1126/science.abb3363)
- Mirabel, I. F., Claret, A., Cesarsky, C. J., Boulade, O., & Cesarsky, D. A. 1996, *A&A*, 315, L113
- Mirabel, I. F., & Rodríguez, L. F. 1999, *ARA&A*, 37, 409, doi: [10.1146/annurev.astro.37.1.409](https://doi.org/10.1146/annurev.astro.37.1.409)
- Murase, K. 2012, *ApJL*, 745, L16, doi: [10.1088/2041-8205/745/2/L16](https://doi.org/10.1088/2041-8205/745/2/L16)
- Murase, K. 2018, *PhRvD*, 97, 081301, doi: [10.1103/PhysRevD.97.081301](https://doi.org/10.1103/PhysRevD.97.081301)
- Murase, K. 2022, *ApJL*, 941, L17, doi: [10.3847/2041-8213/aca53c](https://doi.org/10.3847/2041-8213/aca53c)
- Murase, K. 2024, *PhRvD*, 109, 103020, doi: [10.1103/PhysRevD.109.103020](https://doi.org/10.1103/PhysRevD.109.103020)
- Murase, K., Guetta, D., & Ahlers, M. 2016, *PhRvL*, 116, 071101, doi: [10.1103/PhysRevLett.116.071101](https://doi.org/10.1103/PhysRevLett.116.071101)
- Murase, K., Kashiyama, K., Kiuchi, K., & Bartos, I. 2015, *ApJ*, 805, 82, doi: [10.1088/0004-637X/805/1/82](https://doi.org/10.1088/0004-637X/805/1/82)
- Murase, K., Kashiyama, K., & Mészáros, P. 2013, *PhRvL*, 111, 131102, doi: [10.1103/PhysRevLett.111.131102](https://doi.org/10.1103/PhysRevLett.111.131102)
- Murase, K., Kimura, S. S., & Mészáros, P. 2020, *PhRvL*, 125, 011101, doi: [10.1103/PhysRevLett.125.011101](https://doi.org/10.1103/PhysRevLett.125.011101)
- Murase, K., & Waxman, E. 2016, *PhRvD*, 94, 103006, doi: [10.1103/PhysRevD.94.103006](https://doi.org/10.1103/PhysRevD.94.103006)
- Ogley, R. N., Bell Burnell, S. J., & Fender, R. P. 2001, *MNRAS*, 322, 177, doi: [10.1046/j.1365-8711.2001.04129.x](https://doi.org/10.1046/j.1365-8711.2001.04129.x)
- Ohira, Y. 2025, *MNRAS*, 541, 2434, doi: [10.1093/mnras/staf1176](https://doi.org/10.1093/mnras/staf1176)
- Pandey, M., Rao, A. P., Pooley, G. G., et al. 2006, *A&A*, 447, 525, doi: [10.1051/0004-6361:20053437](https://doi.org/10.1051/0004-6361:20053437)
- Parker, M. L., Tomsick, J. A., Miller, J. M., et al. 2015, *ApJ*, 808, 9, doi: [10.1088/0004-637X/808/1/9](https://doi.org/10.1088/0004-637X/808/1/9)
- Pepe, C., Vila, G. S., & Romero, G. E. 2015, *A&A*, 584, A95, doi: [10.1051/0004-6361/201527156](https://doi.org/10.1051/0004-6361/201527156)
- Peretti, E., Petropoulou, M., Vasilopoulos, G., & Gabici, S. 2025, *A&A*, 698, A188, doi: [10.1051/0004-6361/202452987](https://doi.org/10.1051/0004-6361/202452987)
- Persi, P., Ferrari-Toniolo, M., Grasdalen, G. L., & Spada, G. 1980, *A&A*, 92, 238
- Prabu, S., Miller-Jones, J. C. A., Bahramian, A., et al. 2025, *arXiv e-prints*, arXiv:2512.09645, doi: [10.48550/arXiv.2512.09645](https://doi.org/10.48550/arXiv.2512.09645)
- Rachen, J. P., & Mészáros, P. 1998, *PhRvD*, 58, 123005, doi: [10.1103/PhysRevD.58.123005](https://doi.org/10.1103/PhysRevD.58.123005)
- Reid, M. J., & Miller-Jones, J. C. A. 2023, *ApJ*, 959, 85, doi: [10.3847/1538-4357/acfe0c](https://doi.org/10.3847/1538-4357/acfe0c)
- Reynoso, M. M., & Romero, G. E. 2009, *A&A*, 493, 1, doi: [10.1051/0004-6361:200811004](https://doi.org/10.1051/0004-6361:200811004)
- Reynoso, M. M., Romero, G. E., & Christiansen, H. R. 2008, *MNRAS*, 387, 1745, doi: [10.1111/j.1365-2966.2008.13364.x](https://doi.org/10.1111/j.1365-2966.2008.13364.x)
- Ribó, M. 2005, in *Astronomical Society of the Pacific Conference Series*, Vol. 340, *Future Directions in High Resolution Astronomy*, ed. J. Romney & M. Reid, 269, doi: [10.48550/arXiv.astro-ph/0402134](https://doi.org/10.48550/arXiv.astro-ph/0402134)
- Rushton, A., Miller-Jones, J. C. A., Campana, R., et al. 2012, *MNRAS*, 419, 3194, doi: [10.1111/j.1365-2966.2011.19959.x](https://doi.org/10.1111/j.1365-2966.2011.19959.x)
- Sabatini, S., Tavani, M., Coppi, P., et al. 2013, *ApJ*, 766, 83, doi: [10.1088/0004-637X/766/2/83](https://doi.org/10.1088/0004-637X/766/2/83)
- Schaerer, D. 1996, *A&A*, 309, 129, doi: [10.48550/arXiv.astro-ph/9509079](https://doi.org/10.48550/arXiv.astro-ph/9509079)
- Schneider, N., Bontemps, S., Simon, R., et al. 2006, *A&A*, 458, 855, doi: [10.1051/0004-6361:20065088](https://doi.org/10.1051/0004-6361:20065088)
- Shibata, S., Tomatsuri, H., Shimanuki, M., Saito, K., & Mori, K. 2003, *MNRAS*, 346, 841, doi: [10.1111/j.1365-2966.2003.07131.x](https://doi.org/10.1111/j.1365-2966.2003.07131.x)
- Stecker, F. W., Harding, A. K., & Barnard, J. J. 1985, *Nature*, 316, 418, doi: [10.1038/316418a0](https://doi.org/10.1038/316418a0)
- Steiner, J. F., Nathan, E., Hu, K., et al. 2024, *ApJL*, 969, L30, doi: [10.3847/2041-8213/ad58e4](https://doi.org/10.3847/2041-8213/ad58e4)
- Stirling, A. M., Spencer, R. E., de la Force, C. J., et al. 2001, *MNRAS*, 327, 1273, doi: [10.1046/j.1365-8711.2001.04821.x](https://doi.org/10.1046/j.1365-8711.2001.04821.x)

- Svensson, R. 1987, *MNRAS*, 227, 403, doi: [10.1093/mnras/227.2.403](https://doi.org/10.1093/mnras/227.2.403)
- Szostek, A., & Zdziarski, A. A. 2007, *MNRAS*, 375, 793, doi: [10.1111/j.1365-2966.2006.11346.x](https://doi.org/10.1111/j.1365-2966.2006.11346.x)
- Szostek, A., Zdziarski, A. A., & McCollough, M. L. 2008, *MNRAS*, 388, 1001, doi: [10.1111/j.1365-2966.2008.13479.x](https://doi.org/10.1111/j.1365-2966.2008.13479.x)
- Tananbaum, H., Gursky, H., Kellogg, E., Giacconi, R., & Jones, C. 1972, *ApJL*, 177, L5, doi: [10.1086/181042](https://doi.org/10.1086/181042)
- Tetarenko, A. J., Casella, P., Miller-Jones, J. C. A., et al. 2019, *MNRAS*, 484, 2987, doi: [10.1093/mnras/stz165](https://doi.org/10.1093/mnras/stz165)
- Tomsick, J. A., Parker, M. L., García, J. A., et al. 2018, *ApJ*, 855, 3, doi: [10.3847/1538-4357/aaaab1](https://doi.org/10.3847/1538-4357/aaaab1)
- van Kerkwijk, M. H., Charles, P. A., Geballe, T. R., et al. 1992, *Nature*, 355, 703, doi: [10.1038/355703a0](https://doi.org/10.1038/355703a0)
- Veledina, A., Muleri, F., Poutanen, J., et al. 2024, *Nature Astronomy*, 8, 1031, doi: [10.1038/s41550-024-02294-9](https://doi.org/10.1038/s41550-024-02294-9)
- Vilhu, O., Koljonen, K. I. I., & Hannikainen, D. C. 2023, *A&A*, 674, A74, doi: [10.1051/0004-6361/202346125](https://doi.org/10.1051/0004-6361/202346125)
- Wang, J., Reville, B., & Aharonian, F. A. 2025, *ApJL*, 989, L25, doi: [10.3847/2041-8213/adf3a4](https://doi.org/10.3847/2041-8213/adf3a4)
- Werner, G. R., Uzdensky, D. A., Cerutti, B., Nalewajko, K., & Begelman, M. C. 2016, *ApJL*, 816, L8, doi: [10.3847/2041-8205/816/1/L8](https://doi.org/10.3847/2041-8205/816/1/L8)
- Yañez, J. P., & Fedynitch, A. 2023, *PhRvD*, 107, 123037, doi: [10.1103/PhysRevD.107.123037](https://doi.org/10.1103/PhysRevD.107.123037)
- Yuan, F., & Narayan, R. 2014, *ARA&A*, 52, 529, doi: [10.1146/annurev-astro-082812-141003](https://doi.org/10.1146/annurev-astro-082812-141003)
- Zanin, R., Fernández-Barral, A., de Oña Wilhelmi, E., et al. 2016, *A&A*, 596, A55, doi: [10.1051/0004-6361/201628917](https://doi.org/10.1051/0004-6361/201628917)
- Zdziarski, A. A. 2012, *MNRAS*, 422, 1750, doi: [10.1111/j.1365-2966.2012.20754.x](https://doi.org/10.1111/j.1365-2966.2012.20754.x)
- Zdziarski, A. A., Malyshev, D., Chernyakova, M., & Pooley, G. G. 2017, *MNRAS*, 471, 3657, doi: [10.1093/mnras/stx1846](https://doi.org/10.1093/mnras/stx1846)
- Zdziarski, A. A., Sikora, M., Dubus, G., et al. 2012, *MNRAS*, 421, 2956, doi: [10.1111/j.1365-2966.2012.20519.x](https://doi.org/10.1111/j.1365-2966.2012.20519.x)
- Zdziarski, A. A., Malyshev, D., Dubus, G., et al. 2018, *MNRAS*, 479, 4399, doi: [10.1093/mnras/sty1618](https://doi.org/10.1093/mnras/sty1618)
- Zhang, B. T., Kimura, S. S., & Murase, K. 2025, *Phys. Rev. D*, 112, 123015, doi: [10.1103/p6r1-qg5q](https://doi.org/10.1103/p6r1-qg5q)
- Zhang, B. T., & Murase, K. 2023, *MNRAS*, 524, 76, doi: [10.1093/mnras/stad1829](https://doi.org/10.1093/mnras/stad1829)
- Zhang, B. T., Murase, K., Veres, P., & Mészáros, P. 2021, *ApJ*, 920, 55, doi: [10.3847/1538-4357/ac0cfc](https://doi.org/10.3847/1538-4357/ac0cfc)
- Zhang, S.-N. 2013, *Frontiers of Physics*, 8, 630, doi: [10.1007/s11467-013-0306-z](https://doi.org/10.1007/s11467-013-0306-z)
- Ziótkowski, J. 2005, *MNRAS*, 358, 851, doi: [10.1111/j.1365-2966.2005.08796.x](https://doi.org/10.1111/j.1365-2966.2005.08796.x)